Comparison of Eigenvectors for Coupled Seismo-Electromagnetic Layered-Earth Modeling

Grobbe, Niels; Slob, Evert; Thorbecke, Jan Willem

Important note
To cite this publication, please use the final published version (if applicable).
Please check the document version above.

Comparison of eigenvectors for coupled seismo-electromagnetic layered-Earth modelling

N. Grobbe, E.C. Slob and J.W. Thorbecke

Delft University of Technology, Department of Geoscience and Engineering, 2628 *CN Delft, The Netherlands. E-mail:* ngrobbe@gmail.com

SUMMARY

We study the accuracy and numerical stability of three eigenvector sets for modelling the coupled poroelastic and electromagnetic layered-Earth response. We use a known eigenvector set, its flux-normalized version and a newly derived flux-normalized set. The new set is chosen such that the system is properly uncoupled when the coupling between the poroelastic and electromagnetic fields vanishes. We carry out two different numerical stability tests: the first test focuses on the internal system, eigenvector and eigenvalue consistency; the second test investigates the stability and preciseness of the flux-normalized systems by looking at identity relations. We find that the known set shows the largest deviation for both tests, whereas the new set performs best. In two additional numerical modelling experiments, these numerical inaccuracies are shown to generate numerical noise levels comparable to small signals, such as signals coming from the important interface conversion responses, especially when the coupling coefficient is small. When coupling vanishes completely, the known set does not produce proper results. The new set produces numerically stable and accurate results in all situations. We therefore strongly recommend to use this newly derived set for future layered-Earth seismo-electromagnetic modelling experiments.

Key words: Numerical solutions; Electromagnetic theory; Magnetic and electrical properties; Theoretical seismology; Wave propagation; Acoustic properties.

1 INTRODUCTION

Applied geophysics is concerned with subsurface imaging and characterization using data measured at or below the Earth's surface. Increasing societal challenges such as environmental issues or the quest for natural resources have sparked the continuous search for improved imaging and characterization techniques. In this light, many researchers have investigated the potential of coupled seismo-electromagnetic wavefields for geophysical exploration, imaging, and monitoring (Frenkel 1944; Pride & Morgan 1991; Thompson & Gist 1993; Pride 1994; Jouniaux & Pozzi 1995; Butler *et al.* 1996; Zhu *et al.* 2000; Garambois & Dietrich 2002; Haines & Pride 2006; Hu *et al.* 2007; Dean & Dupuis 2011; Schakel *et al.* 2011; Sava & Revil 2012; Smeulders *et al.* 2014; Revil *et al.* 2015; Grobbe & Slob 2016). The seismo-electromagnetic effect is described by the coupling between seismic waves and electromagnetic fields in porous media (partially or fully saturated). In addition, it has been studied in the context of earthquake precursors (Fujinawa *et al.* 2011; Hu & Gao 2011; Ren *et al.* 2012; Fujinawa & Noda 2016). It has the potential to offer complementary information to conventional seismics or conventional controlled-source electromagnetics. Due to the coupling between the elastodynamic wavefields and the electromagnetic fields, the seismo-electromagnetic signals may provide both seismic resolution and electromagnetic fluid-sensitivity at the same time (Schoemaker *et al.* 2012). The coefficient that couples the two wavefields, the seismo-electromagnetic coupling coefficient, contains high-value reservoir information such as the porosity and permeability of the medium (Jardani *et al.* 2010).

We can distinguish two types of coupling in the seismo-electromagnetic phenomena (Garambois & Dietrich 2002; Revil *et al.* 2015). The first is the coupling that occurs 'inside' the seismic wave or electromagnetic field, which is referred to as the coseismic electromagnetic field or the coelectromagnetic mechanical field, respectively. This field contains information at the location where the wave passes and is recorded, that is, at the receivers. The second type of coupling occurs when such a field encounters an interface with contrasting medium parameters. An incident electromagnetic field or seismic wave reflects from and transmits through such an interface both electromagnetic and seismic wavefields. The seismo-electromagnetic conversion that occurs here, contains information about medium properties at depth and is generally of most interest to geophysicists. This effect is also referred to as the interface response field. In addition, seismo-electromagnetic conversion occurs directly at the source.

One of the main difficulties when trying to apply seismo-electromagnetic techniques in the field is the small amplitude of the seismo-electromagnetic conversions, especially the interface response fields. Even if the signals would be stronger, the fact remains that the seismo-electromagnetic effect is a very complex physical field and hard to fully understand.

Our knowledge of the seismo-electromagnetic fields has increased substantially due to theoretical, numerical and laboratory experiments, as well as field tests. A great contribution to seismo-electromagnetic theory was done by Pride (1994), who derived a set of governing equations describing the coupled seismo-electromagnetic system in fully saturated, porous media, using the principle of volume averaging. He started from Biot's poroelasticity theory and Maxwell's electromagnetic equations and combined them using a volume averaging technique. As a next step, Haartsen & Pride (1997) derived a set of eigenvectors for modelling seismo-electromagnetic wavefields in horizontally layered, 1-D media. To model 2-D and 3-D media, finite-difference (Haines & Pride 2006) and finite-element schemes (Zyserman *et al.* 2010) have been developed. Applying acoustic geophysical processing, imaging and inversion techniques to seismo-electromagnetic data can be challenging, but is not impossible (Jardani *et al.* 2010; Mahardika *et al.* 2012; Maas *et al.* 2015). More specifically dedicated seismo-electromagnetic processing is discussed in, for example, Warden *et al.* (2012).

In the seismo-electromagnetic theory as described by Pride (1994), Biot's poroelasticity equations are coupled to Maxwell's electromagnetic equations, where full coupling between the electric and magnetic fields is considered. An alternative formulation makes use of the well-known quasi-static approach, exploiting the fact that at low-frequency, the electric and magnetic parts are not coupled. In this approach, the electric field can be written as minus the gradient of an electrical potential. Important works exploiting this formulation include Revil *et al.* (2003), Haines & Pride (2006), Jardani *et al.* (2010), Zyserman *et al.* (2010), Jougnot *et al.* (2013), Monachesi *et al.* (2015) and Revil *et al.* (2015). Considering the amount of parameters that are involved in describing the seismo-electromagnetic effect, simplifying the system of equations is proven beneficial for both our understanding of the phenomenon as well as for further developing the technique towards imaging and inversion (Jardani *et al.* 2010; Mahardika *et al.* 2012; Sava & Revil 2012; Revil *et al.* 2015). For this approximation, a frequency-limit holds that depends on the measurement configuration and the target depth. Recently, Revil & Mahardika (2013) have presented an elegant alternative to the fully coupled theory of Pride (1994), that also allows to study seismo-electromagnetic effects in unsaturated porous media, and even two-phase flow media (Jardani & Revil 2015). Coupling in partially saturated media has also been studied following the theory as developed by Pride (1994), and is nicely presented in Warden *et al.* (2013).

In this paper, we study the numerical stability and its impact on seismo-electromagnetic records. We desire that all coupling effects (even very weak effects) are taken into account in our modelling. To this end, we do not want to make any approximations regarding the Maxwell equations, and prefer to model the fully coupled Maxwell equations. We therefore focus on modelling in layered media using the theory as developed by Pride (1994).

Besides numerical studies, laboratory studies have been carried out in attempts to better understand the electrokinetic foundations, the seismo-electromagnetic phenomenon itself and the responses that are to be expected (Jouniaux & Pozzi 1995; Allègre *et al.* 2010; Zhu *et al.* 2000; Zhu & Toksöz 2005). By comparing laboratory experiments with theoretical models, several aspects of electrokinetic and seismo-electromagnetic theory have been validated (Bordes *et al.* 2008; Schakel & Smeulders 2010; Schakel *et al.* 2011; Schoemaker *et al.* 2012; Smeulders *et al.* 2014). However, from all laboratory studies still no convincing match has been obtained between modelled and measured data on actual rock samples. For single and multiple cylindrical pores in a sample, good results have been obtained validating the analytical models for the transport equations (Schoemaker *et al.* 2012).

When considering a medium that is invariant in two directions, it is useful to decouple the total 3-D seismo-electromagnetic system of equations into two independent propagation modes, the SH-TE mode and the P-SV-TM mode. In the SH-TE mode, the horizontally polarized shear waves (SH) are coupled to the transverse electric mode (TE), and in the P-SV-TM mode the fast and slow compressional waves (P) are coupled to the transverse magnetic mode (TM) through the vertically polarized shear waves (SV; Haartsen & Pride 1997; Grobbe *et al.* 2016). Decoupling enables us to treat the SH-TE system and the P-SV-TM system independently of each other. In other words, each seismo-electromagnetic propagation mode can be described by its own, independent eigenvector set. These two independent eigenvector sets are the basis of seismo-electromagnetic numerical modelling codes for layered-Earth models (Haartsen & Pride 1997; Garambois & Dietrich 2002; Ren *et al.* 2010; Grobbe & Slob 2013). Eigenvectors are non-uniquely defined, since different normalization factors can be applied to the system. The first set of eigenvectors was presented by Haartsen & Pride (1997), and used by Garambois & Dietrich (2002), where they applied displacement-normalization for the SH-TE mode. They have briefly mentioned alternative normalization possibilities as well, for example, normalization based on power, referred to as power-flux normalization. The power-flux normalization yields favourable reciprocity relations for the flux-normalized one-way fields as well as numerical advantages (see e.g. Frasier 1970; Wapenaar 1998, and for a discussion on field decomposition Grobbe *et al.* 2016).

Over the last couple of years, we have developed an analytically based, numerical modelling code called 'ESSEMOD', which stands for electromagneto-seismic and seismo-electromagnetic modelling (Grobbe *et al.* 2012, 2014). In contrast to other existing layered-Earth modelling codes, our modelling code is capable of modelling all existing seismo-electromagnetic and electromagneto-seismic source–receiver combinations for homogeneous layered media. At the source level, the two-way wavefields are decomposed into upgoing and downgoing one-way wavefields, which are extrapolated via one-way wavefield extrapolation operators in the horizontal wavenumber–frequency domain (Wapenaar & Berkhout 1989; Grobbe 2016; Grobbe *et al.* 2016). The code makes use of global reflection scheme (based on the three-layer scalar reflection scheme by Airy (1833)), leading to an efficient numerical scheme due to the fact that explicit calculation of the scattering matrices is not required (Grobbe 2016). In this scheme, we distinguish local reflection matrices from global reflection matrices. Both the

expressions for the local and the global reflection matrices make use of combinations of eigenvectors, with the medium properties of the media that are separated by the interface under consideration. The term local reflection matrix indicates that these matrices only account for one reflection at one specific interface. To account for all multiple reflections, global reflection matrices are developed, that exploit wavefield extrapolation operators. At the receiver level, wavefield composition takes place using eigenvector-based composition matrices. Additionally, the independently treated SH-TE and P-SV-TM propagation modes are combined, resulting in two-way wavefields due to two-way sources. We then apply Fourier–Bessel transformations to efficiently transform the data from the horizontal wavenumber–frequency domain to the space-frequency domain.

It is evident that eigenvectors play a crucial role in the whole algorithm of ESSEMOD, and any layered-Earth modelling code. In this paper, we study the numerical stability of three different seismo-electromagnetic eigenvector sets. We start with the seismo-electromagnetic system as described by Pride (1994), captured and organized in the system matrix and notation according to our preferences. We present the first eigenvector system of Haartsen & Pride (1997) and show how we can easily flux-normalize this system of equations, leading to the second eigenvector set. We then present our independently derived alternative eigenvector sets for both the SH-TE and P-SV-TM propagation modes. We show how any desired eigenvector set (e.g. a system that is properly uncoupled when the coupling between the poroelastic and electromagnetic fields vanishes) can be derived starting from the system matrices and the eigenvalue matrices. The presented derivation can in principle be applied to any physical wave or field phenomenon that is captured in a certain matrix-vector representation of the two-way wave equation. This is useful, especially for larger systems such as poroelastic systems or the here presented seismo-electromagnetic system. It is shown that the derivation does not depend on which eigenvector scaling is applied, and that in the final stages the scaling factor can still be adjusted according to preference. We then numerically compare the three different eigenvector sets: the set of Haartsen & Pride (1997) (adjusted to our preferences and referred to as the 'HP' eigenvector set), the power-flux normalized version of this set derived starting from the adjusted Haartsen & Pride (1997) set (referred to as the 'HPF' eigenvector set) and third our independently derived alternative power-flux normalized eigenvector set starting directly from the system matrix itself (referred to as the 'GST' eigenvector set). The two numerical stability tests focus on system consistency and flux-normalization properties. Clear differences in numerical stability and precision are observed, where the GST set performs consistently better than the HP and HPF set. We demonstrate theoretically and numerically that when the seismo-electromagnetic coupling coefficient is equal to zero (i.e. when there is no coupling between mechanical and electromagnetic fields), our set correctly models the decoupled purely poroelastic and purely electromagnetic systems, whereas the HP and HPF sets fail. We present a numerical validation of all three eigenvector sets, followed by two numerical examples demonstrating that the differences in numerical stability and accuracy have obvious implications on finding small amplitude signals when there are also strong signals in the data. Where the HP and HPF sets break down, our newly developed GST set models all events accurately at all times.

2 THEORY

2.1 Seismo-electromagnetic equations in a general two-way field equation format

The set of macroscopic governing equations for the seismo-electromagnetic system in an arbitrary inhomogeneous fluid-saturated porous medium were derived by Pride (1994). We adopt this set of equations, using an opposite definition of the Fourier Transform and expressing the mechanical fields in terms of particle velocity instead of displacement. For the purpose of this paper, we will not recapitulate this extensive theory in our notation and do not discuss all the parameters and their mutual relations in great detail. The details can be found in Grobbe (2016).

Throughout this paper we use

$$\hat{f}(x_i, \omega) = \int_{-\infty}^{\infty} f(x_i, t) e^{-j\omega t} dt \tag{1}$$

as the definition for the forward temporal Fourier transform, and

$$\tilde{f}(k_1, k_2, x_3, \omega) = \int_{-\infty}^{\infty} \int_{-\infty}^{\infty} \hat{f}(x_i, \omega) e^{jk_\alpha x_\alpha} dx_1 dx_2 \tag{2}$$

for the forward spatial Fourier transform. Here, ω denotes the angular frequency in (rad s^{-1}], t is time, j indicates the imaginary number, x_i indicates the three spatial directions of the right-handed Cartesian coordinate system (with the positive x_3-direction pointing downwards (depth)), and k_α, with $\alpha = 1$ or 2, denotes the horizontal wavenumber in those respective directions. The hat indicates a quantity in the space-frequency domain, the tilde sign indicates a quantity in the horizontal wavenumber–frequency domain. Latin subscripts can take the values 1, 2 and 3, Greek subscripts can take the values 1 and 2. The Einstein summation convention holds for repeated indices (unless indicated otherwise).

Since we are considering a medium that is invariant in two directions (layered-Earth), it is useful to decouple the total 3-D system of seismo-electromagnetic equations into two independent propagation modes: the SH-TE and the P-SV-TM propagation mode. In the Earth, the major variations occur in the depth direction. It therefore makes sense to choose the vertical axis as the direction of preference and

express the vertical variations of the fields in terms of the horizontal variations of the fields (Haartsen & Pride 1997; Grobbe 2016; Grobbe *et al.* 2016). We can then capture this system of equations in the following matrix–vector representation of the two-way wave equation in the space-frequency domain, for both propagation modes independently:

$$\frac{\partial \hat{\mathbf{q}}^{H,V}(\mathbf{x}, \omega)}{\partial x_3} = \hat{\mathbf{A}}^{H,V}(\mathbf{x}, \omega)\hat{\mathbf{q}}^{H,V}(\mathbf{x}, \omega) + \hat{\mathbf{d}}^{H,V}(\mathbf{x}, \omega). \tag{3}$$

The superscripts H and V indicate whether we are dealing with the SH-TE system or the P-SV-TM system, respectively. This two-way wave equation format can be used for a variety of waves and fields (Wapenaar *et al.* 2008). Eq. (3) expresses, in matrix-vector notation indicated by the boldface symbols, the vertical variations of the field quantities in $\hat{\mathbf{q}}^{H,V}(\mathbf{x}, \omega)$, in terms of the medium parameters and the horizontal partial derivative operators of system matrix $\hat{\mathbf{A}}^{H,V}(\mathbf{x}, \omega)$ that act on these field quantities (Woodhouse 1974; Kennett 1983; Ursin 1983; Wapenaar & Grimbergen 1996). Furthermore, $\hat{\mathbf{d}}^{H,V}(\mathbf{x}, \omega)$ represents the source vector containing all source terms of the seismo-electromagnetic SH-TE and P-SV-TM modes. The field quantities for each of these modes in $\hat{\mathbf{q}}^{H,V}$ are continuous across horizontal interfaces. We here present the final field vectors, system matrices and source vectors for both the SH-TE and P-SV-TM systems (details can be found in Haartsen & Pride 1997; Grobbe 2016). We express our equations in the horizontal wavenumber–frequency domain, meaning that we capture both propagation modes in the following two-way wave equation

$$\frac{\partial \tilde{\mathbf{q}}^{H,V}(\mathbf{k}_H, x_3, \omega)}{\partial x_3} = \tilde{\mathbf{A}}^{H,V}(\kappa, x_3, \omega)\tilde{\mathbf{q}}^{H,V}(\mathbf{k}_H, x_3, \omega) + \tilde{\mathbf{d}}^{H,V}(\mathbf{k}_H, x_3, \omega), \tag{4}$$

where $\kappa = \sqrt{k_1^2 + k_2^2}$ denotes the radial wavenumber and $\mathbf{k}_H = (k_1, k_2)$ is the horizontal wavenumber vector. Since we prefer the system to be power-flux normalized, we have reorganized the governing system of equations in such a way that we obtain an optimal symmetry to apply the power-flux normalization (see for details on power-flux normalization e.g. Ursin 1983). Note that this is a different organization compared to Haartsen & Pride (1997).

2.1.1 SH-TE propagation mode

Let us start by introducing a more compact notation for seismo-electromagnetic parameter combinations:

$$\alpha = s\hat{\rho}^c \tag{5}$$

$$\hat{\rho}^c = \rho^b - \frac{(\rho^f)^2}{\hat{\rho}^E} \tag{6}$$

$$\hat{\rho}^E = \frac{\eta}{s\hat{k}} \tag{7}$$

$$\chi = s\rho^f \hat{\mathcal{L}} \tag{8}$$

$$\beta = \frac{s}{G^{fr}} \tag{9}$$

$$\zeta = \hat{\sigma}^m + s\mu \tag{10}$$

$$\hat{\eta}^E = \hat{\sigma}^e + s\varepsilon \tag{11}$$

$$\hat{\epsilon} = \varepsilon_0 \varepsilon_r + \frac{\hat{\sigma}^e}{s} - \hat{\rho}^E \hat{\mathcal{L}}^2 = \varepsilon + \frac{\hat{\sigma}^e}{s} - \hat{\rho}^E \hat{\mathcal{L}}^2 = \frac{\hat{\eta}^E}{s} - \hat{\rho}^E \hat{\mathcal{L}}^2 \tag{12}$$

$$\xi = \frac{\eta}{\hat{k}} \hat{\mathcal{L}} = s\hat{\rho}^E \hat{\mathcal{L}} \tag{13}$$

$$\hat{\varsigma} = \hat{\eta}^E - \hat{\xi}\hat{\mathcal{L}} \tag{14}$$

$$\frac{\hat{\eta}^e}{\hat{\varsigma}} = 1 + \frac{\hat{\xi}\hat{\mathcal{L}}}{\hat{\varsigma}}. \tag{15}$$

Here, s is the Laplace parameter $s = j\omega$, ρ^b the frequency-independent, isotropic bulk density, ρ^f the frequency-independent, isotropic fluid density, η the pore fluid viscosity, $\hat{k}$ the frequency-dependent dynamic permeability, $\hat{\mathcal{L}}$ the dynamic seismo-electromagnetic coupling coefficient and G^{fr} the shear modulus of the solid framework. Furthermore, $\hat{\sigma}^m$ and $\hat{\sigma}^e$ describe the frequency-dependent magnetic and electric conductivities, respectively. For Earth materials, we can ignore magnetic relaxation losses, that is, $\hat{\sigma}^m = 0$. In addition, $\varepsilon = \varepsilon_0 \varepsilon_r$ and $\mu = \mu_0 \mu_r$, where ε_0 and μ_0 represent the electric permittivity and the magnetic permeability of vacuum, ε_r the relative electric permittivity, and

μ_r the relative magnetic permeability. We use the following arrangement of the field vector for the SH-TE propagation mode

$$\tilde{\mathbf{q}}^H = \begin{pmatrix} \tilde{\mathbf{q}}_1^H \\ \tilde{\mathbf{q}}_2^H \end{pmatrix} = \begin{pmatrix} \tilde{v}^{s,H} \\ \tilde{E}^H \\ \tilde{\tau}^{b,H} \\ -\tilde{H}^H \end{pmatrix}, \tag{16}$$

where the superscript H indicates that that respective field quantity is an SH-TE mode quantity. The different mode-quantities are defined as follows

$$\tilde{v}^{s,H} = -jk_1\tilde{v}_2^s + jk_2\tilde{v}_1^s \tag{17}$$

$$\tilde{\tau}^{b,H} = -jk_1\tilde{\tau}_{23}^b + jk_2\tilde{\tau}_{13}^b \tag{18}$$

$$\tilde{E}^H = -jk_1\tilde{E}_2 + jk_2\tilde{E}_1 \tag{19}$$

$$\tilde{H}^H = -jk_1\tilde{H}_1 - jk_2\tilde{H}_2. \tag{20}$$

Here, $\tilde{v}_\alpha^s$ denotes the solid particle velocity, τ_{ij}^b the bulk stress tensor (excluding $i = j = 3$), $\tilde{E}_\alpha$ the electric field strength and $\tilde{H}_\alpha$ the magnetic field strength. The corresponding system matrix reads

$$\tilde{\mathbf{A}}^H = \begin{pmatrix} \mathbf{O} & \tilde{\mathbf{A}}_{12} \\ \tilde{\mathbf{A}}_{21} & \mathbf{O} \end{pmatrix}, \tag{21}$$

which consists of anti-diagonal symmetric block matrix operators, reading

$$\tilde{\mathbf{A}}_{12}^H = \begin{pmatrix} \beta & 0 \\ 0 & -\zeta \end{pmatrix}, \tag{22}$$

$$\tilde{\mathbf{A}}_{21}^H = \begin{pmatrix} \alpha + \frac{\kappa^2}{\beta} & \chi \\ \chi & -(\hat{\eta}^E + \frac{\kappa^2}{\zeta}) \end{pmatrix}. \tag{23}$$

In eq. (21), $\mathbf{O}$ is a two-by-two zero-matrix. The SH-TE source vector in the horizontal wavenumber–frequency domain then reads

$$\tilde{\mathbf{d}}^H = \begin{pmatrix} -jk_1\left[\tilde{h}_{23}^b + \tilde{h}_{32}^b\right] + jk_2\left[\tilde{h}_{13}^b + \tilde{h}_{31}^b\right] \\ -jk_\alpha \tilde{J}_\alpha^m \\ jk_1\left[\tilde{f}_2^b - \frac{\rho^f}{\hat{\rho}^E}\tilde{f}_2^f\right] - jk_2\left[\tilde{f}_1^b - \frac{\rho^f}{\hat{\rho}^E}\tilde{f}_1^f\right] + \frac{1}{s}\left[-k_1^2 + k_2^2\right]\left[G^{fr}\tilde{h}_{21}^b + G^{fr}\tilde{h}_{12}^b\right] - \frac{k_1 k_2}{s}\left[-2G^{fr}\tilde{h}_{11}^b + 2G^{fr}\tilde{h}_{22}^b\right] \\ -\hat{\mathcal{L}}\left[-jk_1\tilde{f}_2^f + jk_2\tilde{f}_1^f\right] + jk_1\tilde{J}_2^e - jk_2\tilde{J}_1^e - \frac{1}{s\mu_0}\kappa^2\tilde{J}_3^m \end{pmatrix}. \tag{24}$$

We can recognize the following source types: $\tilde{h}_{ij}^b$ is the density of external deformation rate acting on the bulk (excluding $i = j = 3$), $\tilde{J}_i^m$ represents an external magnetic current source, $\tilde{f}_\alpha^b$ and $\tilde{f}_\alpha^f$ denote the volume densities of external force applied to the bulk and fluid phases, respectively, and $\tilde{J}_\alpha^e$ is an external electric current source.

2.1.2 P-SV-TM propagation mode

For the P-SV-TM propagation mode, we use the following arrangement of the field vector:

$$\tilde{\mathbf{q}}^V = \begin{pmatrix} \tilde{\mathbf{q}}_1^V \\ \tilde{\mathbf{q}}_2^V \end{pmatrix} = \begin{pmatrix} \tilde{v}_3^s \\ \tilde{w}_3 \\ \tilde{\tau}_{\text{norm}}^{b,V} \\ \tilde{H}_{\text{norm}}^V \\ \tilde{\tau}_{33}^b \\ -\tilde{p}^f \\ \tilde{v}_{\text{norm}}^{s,V} \\ \tilde{E}_{\text{norm}}^V \end{pmatrix}, \tag{25}$$

where the superscript V indicates that these field quantities are P-SV-TM mode quantities. They are defined as

$$\tilde{v}_{\text{norm}}^{s,V} = \frac{k_1}{\kappa}\tilde{v}_1^s + \frac{k_2}{\kappa}\tilde{v}_2^s \tag{26}$$

$$\tilde{\tau}^{b,V}_{\text{norm}} = \frac{k_1}{\kappa}\tilde{\tau}^{b}_{13} + \frac{k_2}{\kappa}\tilde{\tau}^{b}_{23} \tag{27}$$

$$\tilde{E}^{V}_{\text{norm}} = \frac{k_1}{\kappa}\tilde{E}_1 + \frac{k_2}{\kappa}\tilde{E}_2 \tag{28}$$

$$\tilde{H}^{V}_{\text{norm}} = \frac{k_1}{\kappa}\tilde{H}_2 - \frac{k_2}{\kappa}\tilde{H}_1. \tag{29}$$

We have normalized the mode quantities of the P-SV-TM mode with a factor $-j\kappa$, such that the system matrix $\tilde{\mathbf{A}}^{V}$ has favourable symmetry properties. In addition to the field quantities of the SH-TE mode, the P-SV-TM mode contains: $\tilde{v}^{s}_3$, denoting the vertical component of the solid particle velocity, $\tilde{w}_3$, being the vertical component of the filtration velocity, τ^{b}_{33}, representing the vertical component of the bulk stress tensor, and $\tilde{p}^{f}$, indicating the fluid pressure.

   This arrangement of the field vector and choice for the normalization results in the following P-SV-TM system matrix

$$\tilde{\mathbf{A}}^{V} = \begin{pmatrix} \mathbf{O} & \tilde{\mathbf{A}}^{V}_{12} \\ \tilde{\mathbf{A}}^{V}_{21} & \mathbf{O} \end{pmatrix}, \tag{30}$$

where the submatrices are defined as

$$\tilde{\mathbf{A}}^{V}_{12} = \begin{pmatrix} \frac{s}{K_c} & -s\frac{C}{MK_c} & \frac{j\kappa S}{K_c} & 0 \\ -s\frac{C}{MK_c} & \frac{s}{M}\left[1+\frac{C^2}{MK_c}\right]+\frac{\hat{k}}{\eta}\kappa^2 & -j\kappa\frac{\rho^f}{\hat{\rho}^E}+j\kappa\frac{C}{M}\left[1-\frac{S}{K_c}\right] & j\kappa\hat{\mathcal{L}} \\ \frac{j\kappa S}{K_c} & -j\kappa\frac{\rho^f}{\hat{\rho}^E}+j\kappa\frac{C}{M}\left[1-\frac{S}{K_c}\right] & \frac{1}{s}\frac{4G_{fr}(S+G_{fr})}{K_c}\kappa^2+s\hat{\rho}^c & \chi \\ 0 & j\kappa\hat{\mathcal{L}} & \chi & -\hat{\eta}^E \end{pmatrix} \tag{31}$$

and

$$\tilde{\mathbf{A}}^{V}_{21} = \begin{pmatrix} s\rho^b & s\rho^f & j\kappa & 0 \\ s\rho^f & \frac{s\hat{\rho}^E\hat{\eta}^E}{\hat{\varsigma}} & 0 & j\kappa\frac{\hat{\xi}}{\hat{\varsigma}} \\ j\kappa & 0 & \beta & 0 \\ 0 & j\kappa\frac{\hat{\xi}}{\hat{\varsigma}} & 0 & -\zeta-\frac{1}{\hat{\varsigma}}\kappa^2 \end{pmatrix}. \tag{32}$$

Here, C and M are static scalar stiffness parameters, and $S = K_G - \frac{2}{3}G^{fr} - \frac{C^2}{M}$, where we can recognize the elastodynamic Lamé constant $\lambda_c = K_G - \frac{2}{3}G^{fr}$, with K_G being Gassmann's bulk modulus. Furthermore, $K_c = S + 2G^{fr}$ and we can relate $HM - C^2 = MK_c$, where the stiffness H can be expressed as $H = K_G + \frac{4}{3}G^{fr}$.

   The corresponding P-SV-TM source vector in the horizontal wavenumber–frequency domain is given by

$$\tilde{\mathbf{d}}^{V} = \begin{pmatrix} \frac{S}{(S+2G^{fr})}\left[\tilde{h}^{b}_{11}+\tilde{h}^{b}_{22}\right]+\tilde{h}^{b}_{33} \\ \frac{j}{s\hat{\rho}^E}k_\alpha\tilde{f}^{f}_\alpha+\frac{C}{M}\left[\tilde{h}^{b}_{11}+\tilde{h}^{b}_{22}\right]\left[1-\frac{S}{(S+2G^{fr})}\right]+\tilde{q}^{i} \\ \frac{1}{\kappa}\frac{\rho^f}{\hat{\rho}^E}k_\alpha\tilde{f}^{f}_\alpha-\frac{1}{\kappa}k_\alpha\tilde{f}^{b}_\alpha-\frac{2j}{s}\frac{k_1k_2}{\kappa}\left[G^{fr}\tilde{h}^{b}_{21}+G^{fr}\tilde{h}^{b}_{12}\right]-\frac{j\kappa}{s}\frac{2G^{fr}S}{(S+2G^{fr})}\left[\tilde{h}^{b}_{11}+\tilde{h}^{b}_{22}\right]-\frac{2jG^{fr}}{s\kappa}\left[k_1^2\tilde{h}^{b}_{11}+k_2^2\tilde{h}^{b}_{22}\right] \\ -\frac{1}{\kappa}\left[\hat{\mathcal{L}}k_\alpha\tilde{f}^{f}_\alpha+k_\alpha\tilde{J}^{e}_\alpha\right] \\ -\tilde{f}^{b}_3 \\ \frac{\hat{\rho}^E}{\hat{\varepsilon}}\hat{\mathcal{L}}\tilde{J}^{e}_3-\tilde{f}^{f}_3 \\ \frac{k_\alpha}{\kappa}\left[\tilde{h}^{b}_{\alpha3}+\tilde{h}^{b}_{3\alpha}\right] \\ \frac{j\kappa}{s\hat{\varepsilon}}\tilde{J}^{e}_3+\frac{1}{\kappa}\left[k_2\tilde{J}^{m}_1-k_1\tilde{J}^{m}_2\right] \end{pmatrix}. \tag{33}$$

In addition to the source quantities defined for the SH-TE mode, we recognize $\tilde{h}^{b}_{33}$, representing the vertical components of the density of external deformation rate acting on the bulk, $\tilde{q}^{i}$ being the volume density of injection rate in the fluid phase, $\tilde{f}^{b}_3$ and $\tilde{f}^{f}_3$ denoting the vertical component volume density of external force applied to the bulk and fluid phases, respectively, and $\tilde{J}^{e}_3$ representing the vertical component of the external electric current source.

2.2 Deriving the eigenvectors

Now that we have specified our field vectors $\tilde{\mathbf{q}}^{H,V}$, system matrices $\tilde{\mathbf{A}}^{H,V}$ and source vectors $\tilde{\mathbf{d}}^{H,V}$ for the SH-TE and P-SV-TM propagation modes, we can move onwards to derive and present the eigenvector sets belonging to this specific arrangement. In this section, we derive the eigenvector sets that form the basis for our numerical modelling examples. Before diving into greater detail, let us first evaluate what this

eigenvector problem looks like in general. The system matrices above are organized such that they obey the following symmetry relation $\{\tilde{\mathbf{A}}^{H,V}\}^t \mathbf{N}^{H,V} = -\mathbf{N}^{H,V}\tilde{\mathbf{A}}^{H,V}$, with

$$\tilde{\mathbf{N}}^{H,V} = \begin{pmatrix} \mathbf{O} & \mathbf{I} \\ -\mathbf{I} & \mathbf{O} \end{pmatrix}, \tag{34}$$

where the submatrices are either size 2-by-2 or 4-by-4 for the SH-TE and P-SV-TM mode, respectively. Here, $\mathbf{I}$ is a diagonal identity submatrix. The system matrix $\tilde{\mathbf{A}}^{H,V}$ can be decomposed into matrices consisting of its eigenvectors and eigenvalues via

$$\tilde{\mathbf{A}}^{H,V} = \tilde{\mathbf{L}}^{H,V}\tilde{\mathbf{\Lambda}}_1^{H,V}\{\tilde{\mathbf{L}}^{H,V}\}^{-1}. \tag{35}$$

Here, $\tilde{\mathbf{L}}^{H,V}$ and $\{\tilde{\mathbf{L}}^{H,V}\}^{-1}$ represent the composition and decomposition matrices, respectively, that consist of the eigenvectors of the SH-TE or P-SV-TM system matrices. The eigenvectors form the basis for wavefield decomposition into one-way wavefields (see Grobbe *et al.* (2016) for a discussion on seismo-electromagnetic field decomposition).

Furthermore, $\tilde{\mathbf{\Lambda}}_1^{H,V}$ is a diagonal matrix consisting of the eigenvalues of the system, that can be written as

$$\tilde{\mathbf{\Lambda}}_1^{H,V} = \begin{pmatrix} -\tilde{\mathbf{\Lambda}}^{H,V} & \mathbf{O} \\ \mathbf{O} & \tilde{\mathbf{\Lambda}}^{H,V} \end{pmatrix}, \tag{36}$$

where

$$\tilde{\mathbf{\Lambda}}^{H} = \begin{pmatrix} \Gamma_{\mathrm{SH}} & 0 \\ 0 & \Gamma_{\mathrm{TE}} \end{pmatrix} \tag{37}$$

and

$$\tilde{\mathbf{\Lambda}}^{V} = \begin{pmatrix} \Gamma_{\mathrm{Pf}} & 0 & 0 & 0 \\ 0 & \Gamma_{\mathrm{Ps}} & 0 & 0 \\ 0 & 0 & \Gamma_{\mathrm{SV}} & 0 \\ 0 & 0 & 0 & \Gamma_{\mathrm{TM}} \end{pmatrix}. \tag{38}$$

The relations between the vertical wavenumbers Γ_w and the spherical wavenumbers γ_w for a certain type of field w are

$$\Gamma_w^2 = \gamma_w^2 + \kappa^2 \tag{39}$$

$$\gamma_w^2 = \Gamma_w^2 - \kappa^2, \tag{40}$$

with

$$\gamma_w = \frac{s}{\hat{c}_w} \tag{41}$$

and where w can be the horizontally polarized shear wave SH, the transverse electric mode TE, the fast compressional wave P_f, the Biot slow compressional wave P_s, the vertically polarized shear wave SV or the transverse magnetic mode TM. In eq. (41), $\hat{c}_w$ represents the complex wave or field velocity for the specific field type w. To determine the eigenvalues of the system, we need to choose the sign of the square root properly. We choose the positive sign of the square root, based on the fact that for the eigenvalue matrix, we desire that $\Re\{\Gamma_w\} > 0$, based on physical wave propagation constraints (Grobbe *et al.* 2016).

Pride & Haartsen (1996) have determined the complex velocities for each field type, which we can rewrite for our field quantities and our definition of the Fourier transform as

$$\hat{c}_{\mathrm{SH}} = \sqrt{\frac{2}{\frac{\hat{\rho}^c}{G^{fr}} + \frac{\zeta\eta^E}{s^2} + \sqrt{\left[\frac{\hat{\rho}^c}{G^{fr}} - \frac{\zeta\eta^E}{s^2}\right]^2 - \frac{4\zeta\chi^2}{s^3 G^{fr}}}}} \tag{42}$$

$$\hat{c}_{\mathrm{TE}} = \sqrt{\frac{2}{\frac{\hat{\rho}^c}{G^{fr}} + \frac{\zeta\eta^E}{s^2} - \sqrt{\left[\frac{\hat{\rho}^c}{G^{fr}} - \frac{\zeta\eta^E}{s^2}\right]^2 - \frac{4\zeta\chi^2}{s^3 G^{fr}}}}} \tag{43}$$

$$\hat{c}_{\mathrm{Pf}} = \sqrt{\frac{2(HM - C^2)}{\hat{v} - \sqrt{\hat{v}^2 - 4(HM - C^2)\left[\rho^b\frac{\hat{\rho}^E\eta^E}{s\hat{c}} - (\rho^f)^2\right]}}} \tag{44}$$

$$\hat{c}_{\mathrm{Ps}} = \sqrt{\frac{2(HM - C^2)}{\hat{v} + \sqrt{\hat{v}^2 - 4(HM - C^2)\left[\rho^b\frac{\hat{\rho}^E\hat{\eta}^E}{\hat{\zeta}} - (\rho^f)^2\right]}}} \tag{45}$$

$$\hat{c}_{SV} = \hat{c}_{SH} \tag{46}$$

$$\hat{c}_{TM} = \hat{c}_{TE}, \tag{47}$$

where $\hat{v} = \rho^b M + \frac{\hat{\rho}^E \hat{\eta}^E H}{\hat{\varsigma}} - 2\rho^f C$. Due to the isotropic and lateral invariance of the medium, the horizontally and vertically polarized shear wave velocities are equal to each other. The same holds for the transverse electric and transverse magnetic (diffusive) velocities. Note that the expressions for the velocities contain divisions by s. Numerically, we stabilized the expressions adding a small imaginary number to the angular frequencies, thereby modelling using complex frequencies and in the final step compensating for this small imaginary part in the inverse temporal Fourier transform. Alternatively, one could model the spherical wavenumbers where this problem does not occur.

Now, we present two different eigenvector sets. The first set we derive starting from the published eigenvector sets by Haartsen & Pride (1997), where we adjust those sets to our field quantities and arrangement of the fields and apply power-flux normalization. The second set we derive starting directly from the system matrices $\tilde{\mathbf{A}}^{H,V}$, thereby paying special attention to the situation of the coupling coefficient being equal to zero. We again apply power-flux normalization in the final stage.

2.2.1 Power flux-normalizing the Haartsen and pride-based eigenvectors

Starting from the eigenvectors as published by Haartsen & Pride (1997), we apply the conversions as displayed in Table 1 to comply with our field quantities and Fourier definitions and to express the eigenvectors in terms of wavenumbers.

Here, p denotes the horizontal slowness and $\tilde{q}_w$ the vertical slowness. Since we are dealing with particle velocity fields whereas Haartsen & Pride (1997) use particle displacement, we need to multiply each of the eigenvectors that are directly related to the displacement $\tilde{u}$ with the Laplace parameter s. In addition, for Haartsen & Pride (1997), the $-$ sign indicates downgoing fields and the $+$ sign denotes upgoing fields (which is an opposite definition compared to our notation). Furthermore, there is a typo in Haartsen & Pride (1997): for the first element of the SV/TM eigenvector set the $\mp$-sign should be a $\pm$-sign.

We arrange the eigenvector elements according to our preferred field vector organizations: eq. (16) for SH-TE and eq. (25) for P-SV-TM. We desire our composition matrix $\tilde{\mathbf{L}}^{H,V}$, where each column corresponds to the eigenvectors of system matrix $\tilde{\mathbf{A}}^{H,V}$ for a certain field type, to be organized as

$$\tilde{\mathbf{L}}^{H,V} = \begin{pmatrix} \tilde{\mathbf{L}}_1^{H,V} & \tilde{\mathbf{L}}_1^{H,V} \\ \tilde{\mathbf{L}}_2^{H,V} & -\tilde{\mathbf{L}}_2^{H,V} \end{pmatrix}. \tag{48}$$

We can find the power-flux normalized eigenvector matrix by requiring that

$$\left\{\tilde{\mathbf{L}}^{H,V}\right\}^{-1} (\kappa, x_3, \omega) = -\left\{\tilde{\mathbf{N}}^{H,V}\right\}^{-1} \left\{\tilde{\mathbf{L}}^{H,V}\right\}^t (\kappa, x_3, \omega)\tilde{\mathbf{N}}^{H,V}. \tag{49}$$

The details on how to derive the SH-TE and P-SV-TM power-flux normalized eigenvector matrices that satisfy this condition are given in the Supporting Information: Appendix F. Through this procedure, we end up with the following SH-TE power-flux normalized composition matrix:

$$\tilde{\mathbf{L}}^H = \begin{pmatrix} sd_1 & sd_2 & sd_1 & sd_2 \\ -\frac{s\mu_0\hat{\rho}^E\hat{\mathcal{L}}G^{fr}\phi_{SH}}{\rho^f}d_1 & -\frac{s\mu_0\hat{\rho}^E\hat{\mathcal{L}}G^{fr}\phi_{TE}}{\rho^f}d_2 & -\frac{s\mu_0\hat{\rho}^E\hat{\mathcal{L}}G^{fr}\phi_{SH}}{\rho^f}d_1 & -\frac{s\mu_0\hat{\rho}^E\hat{\mathcal{L}}G^{fr}\phi_{TE}}{\rho^f}d_2 \\ -\Gamma_{SH}G^{fr}d_1 & -\Gamma_{TE}G^{fr}d_2 & \Gamma_{SH}G^{fr}d_1 & \Gamma_{TE}G^{fr}d_2 \\ -\frac{\Gamma_{SH}\hat{\rho}^E\hat{\mathcal{L}}G^{fr}\phi_{SH}}{\rho^f}d_1 & -\frac{\Gamma_{TE}\hat{\rho}^E\hat{\mathcal{L}}G^{fr}\phi_{TE}}{\rho^f}d_2 & \frac{\Gamma_{SH}\hat{\rho}^E\hat{\mathcal{L}}G^{fr}\phi_{SH}}{\rho^f}d_1 & \frac{\Gamma_{TE}\hat{\rho}^E\hat{\mathcal{L}}G^{fr}\phi_{TE}}{\rho^f}d_2 \end{pmatrix}, \tag{50}$$

with flux-normalization factors

$$d_1^H = \frac{1}{\sqrt{2s\Gamma_{SH}\left[-G^{fr} + \mu_0\left(\frac{\hat{\rho}^E\hat{\mathcal{L}}G^{fr}\phi_{SH}}{\rho^f}\right)^2\right]}} \tag{51}$$

Table 1. Table showing the required conversions when starting from Haartsen & Pride (1997).

Haartsen & Pride (1997)	Our system
ωp	κ
$-j\omega$	s
s_w	$\frac{\gamma_w}{s}$
$j\omega\tilde{q}_w$	$-\Gamma_w$
$\tilde{q}_w$	$\frac{\Gamma_w}{s}$
$\mp$	$\pm$
'Eigenvector related to the field quantity $\tilde{u}$'	'$s \cdot$ eigenvector related to the field quantity $\tilde{u}$'

$$d_2^H = \frac{1}{\sqrt{2s\Gamma_{\text{TE}}\left[-G^{fr} + \mu_0\left(\frac{\hat{\rho}^E\hat{\mathcal{L}}G^{fr}\phi_{\text{TE}}}{\rho^f}\right)^2\right]}}, \tag{52}$$

and where $\phi_{\text{SH, TE}}$ is a certain scaling factor that depends on the field type, defined as

$$\phi_{\text{SH,TE}} = -\frac{\gamma_{\text{SH,TE}}^2 - \frac{s^2\rho^b}{G^{fr}}}{\gamma_{\text{SH,TE}}^2 - \hat{\varsigma}\zeta}. \tag{53}$$

We choose the positive sign of the square root, based on the fact that for the eigenvalue matrix, we desire that $\Re\{\Gamma_w\} > 0$.

Similarly, our final, power flux-normalized P-SV-TM eigenvectors read

$$\tilde{\mathbf{L}}_1^V = \begin{pmatrix} \frac{s\Gamma_{\text{Pf}}}{\gamma_{\text{Pf}}}d_1^V & \frac{s\Gamma_{\text{Ps}}}{\gamma_{\text{Ps}}}d_2^V & \frac{-sj\kappa}{\gamma_{\text{SV}}}d_3^V & \frac{-sj\kappa}{\gamma_{\text{TM}}}d_4^V \\ \frac{s\Gamma_{\text{Pf}}\phi_{\text{Pf}}}{\gamma_{\text{Pf}}}d_1^V & \frac{s\Gamma_{\text{Ps}}\phi_{\text{Ps}}}{\gamma_{\text{Ps}}}d_2^V & \frac{-G^{fr}}{\rho^f}\left(\frac{\gamma_{\text{SV}}^2}{s^2} - \frac{\rho^b}{G^{fr}}\right)\frac{sj\kappa}{\gamma_{\text{SV}}}d_3^V & \frac{-G^{fr}}{\rho^f}\left(\frac{\gamma_{\text{TM}}^2}{s^2} - \frac{\rho^b}{G^{fr}}\right)\frac{sj\kappa}{\gamma_{\text{TM}}}d_4^V \\ -\frac{2G^{fr}j\kappa\Gamma_{\text{Pf}}}{\gamma_{\text{Pf}}}d_1^V & -\frac{2G^{fr}j\kappa\Gamma_{\text{Ps}}}{\gamma_{\text{Ps}}}d_2^V & -\frac{G^{fr}(\Gamma_{\text{SV}}^2+\kappa^2)}{\gamma_{\text{SV}}}d_3^V & -\frac{G^{fr}(\Gamma_{\text{TM}}^2+\kappa^2)}{\gamma_{\text{TM}}}d_4^V \\ 0 & 0 & -\gamma_{\text{SV}}\frac{\hat{\rho}^E}{\rho^f}\hat{\mathcal{L}}G^{fr}\phi_{\text{SV}}d_3^V & -\gamma_{\text{TM}}\frac{\hat{\rho}^E}{\rho^f}\hat{\mathcal{L}}G^{fr}\phi_{\text{TM}}d_4^V \end{pmatrix}, \tag{54}$$

and

$$\tilde{\mathbf{L}}_2^V = \begin{pmatrix} -\gamma_{\text{Pf}}\left(H + \frac{2G^{fr}\kappa^2}{\gamma_{\text{Pf}}^2} + \phi_{\text{Pf}}C\right)d_1^V & -\gamma_{\text{Ps}}\left(H + \frac{2G^{fr}\kappa^2}{\gamma_{\text{Ps}}^2} + \phi_{\text{Ps}}C\right)d_2^V & \frac{2G^{fr}j\kappa\Gamma_{\text{SV}}}{\gamma_{\text{SV}}}d_3^V & \frac{2G^{fr}j\kappa\Gamma_{\text{TM}}}{\gamma_{\text{TM}}}d_4^V \\ -\gamma_{\text{Pf}}\left(C + \phi_{\text{Pf}}M\right)d_1^V & -\gamma_{\text{Ps}}\left(C + \phi_{\text{Ps}}M\right) & 0 & 0 \\ \frac{sj\kappa}{\gamma_{\text{Pf}}} & \frac{sj\kappa}{\gamma_{\text{Ps}}}d_2^V & \frac{s\Gamma_{\text{SV}}}{\gamma_{\text{SV}}}d_3^V & \frac{s\Gamma_{\text{TM}}}{\gamma_{\text{TM}}}d_4^V \\ \frac{-\hat{\rho}^E\hat{\mathcal{L}}\phi_{\text{Pf}}sj\kappa}{\gamma_{\text{Pf}}\hat{\epsilon}}d_1^V & \frac{-\hat{\rho}^E\hat{\mathcal{L}}\phi_{\text{Ps}}sj\kappa}{\gamma_{\text{Ps}}\hat{\epsilon}}d_2^V & -\frac{\Gamma_{\text{SV}}\mu_0\frac{\hat{\rho}^E}{\rho^f}\hat{\mathcal{L}}G^{fr}\phi_{\text{SV}}s}{\gamma_{\text{SV}}}d_3^V & -\frac{\Gamma_{\text{TM}}\mu_0\frac{\hat{\rho}^E}{\rho^f}\hat{\mathcal{L}}G^{fr}\phi_{\text{TM}}s}{\gamma_{\text{TM}}}d_4^V \end{pmatrix}, \tag{55}$$

where ϕ_w is again a certain scaling factor, depending on the wavetypes w, defined as

$$\phi_{\text{Pf,Ps}} = -\frac{s^2\rho^b - H\gamma_{\text{Pf,Ps}}^2}{s^2\rho^f - C\gamma_{\text{Pf,Ps}}^2}, \tag{56}$$

and where $\phi_{\text{SV, TM}}$ is equal to the scaling factor discussed for the SH-TE mode, eq. (53). The power flux-normalization factors are

$$d_1^V = \frac{1}{\sqrt{2s\Gamma_{\text{Pf}}\left(-H - 2\phi_{\text{Pf}}C - \phi_{\text{Pf}}^2M\right)}} \tag{57}$$

$$d_2^V = \frac{1}{\sqrt{2s\Gamma_{\text{Ps}}\left(-H - 2\phi_{\text{Ps}}C - \phi_{\text{Ps}}^2M\right)}} \tag{58}$$

$$d_3^V = \frac{1}{\sqrt{2s\Gamma_{\text{SV}}\left(-G^{fr} + \mu_0\left[\frac{\hat{\rho}^E\hat{\mathcal{L}}G^{fr}\phi_{\text{SV}}}{\rho^f}\right]^2\right)}} \tag{59}$$

$$d_4^V = \frac{1}{\sqrt{2s\Gamma_{\text{TM}}\left(-G^{fr} + \mu_0\left[\frac{\hat{\rho}^E\hat{\mathcal{L}}G^{fr}\phi_{\text{TM}}}{\rho^f}\right]^2\right)}}, \tag{60}$$

where we recognize identical factors for SH versus SV, and TE versus TM, eqs (51) versus (59), and (52) versus (60), respectively. Again, we choose the positive sign of the square root.

We can observe that when the seismo-electromagnetic coupling coefficient $\hat{\mathcal{L}}$ is equal to zero, the fourth row of composition submatrix, eq. (54), and the fourth row of composition submatrix, eq. (55), are zero for all elements. These rows are involved when composing the two-way electromagnetic P-SV-TM mode field quantities ($\tilde{H}_{\text{norm}}^V$ and $\tilde{E}_{\text{norm}}^V$, respectively) from one-way wavefields, via $\tilde{\mathbf{q}}^V = \tilde{\mathbf{L}}^V\tilde{\mathbf{p}}$, where $\tilde{\mathbf{p}}^V$ contains the downgoing and upgoing wavefields (see also, for example, Grobbe *et al.* 2016). When there is no coupling between mechanical and electromagnetic fields, we expect columns one, two, and three of the composition submatrices in eqs (54) and (55), to be equal to zero, whereas the fourth column (corresponding to the TM field type) should be non-zero, generating the electromagnetic fields. We can see in the composition submatrices, that for the Haartsen & Pride (1997)-based eigenvector set, also this fourth column is equal to zero. Furthermore, we can observe that the fourth, electromagnetically associated column is non-zero for most of the other rows (which correspond to mechanical field quantities) when there is no seismo-electromagnetic coupling. This is physically not what we expect. We investigate numerically the zero-valued coupling coefficient scenario more closely later on.

Looking at eq. (48), it can be observed that the general decomposition matrix $\left\{\tilde{\mathbf{L}}^{H,V}\right\}^{-1}$ can be written as

$$\left\{\tilde{\mathbf{L}}^{H,V}\right\}^{-1} == \frac{1}{2}\begin{pmatrix} \left\{\tilde{\mathbf{L}}_1^{H,V}\right\}^{-1} & \left\{\tilde{\mathbf{L}}_2^{H,V}\right\}^{-1} \\ \left\{\tilde{\mathbf{L}}_1^{H,V}\right\}^{-1} & -\left\{\tilde{\mathbf{L}}_2^{H,V}\right\}^{-1} \end{pmatrix}. \tag{61}$$

However, using eq. (49), we can determine the power-flux normalized decomposition matrix. In a general notation, this power-flux normalized decomposition matrix is organized as follows

$$\left\{\tilde{\mathbf{L}}^{H,V}\right\}^{-1} = \begin{pmatrix} \left\{\tilde{\mathbf{L}}_2^{H,V}\right\}^t & \left\{\tilde{\mathbf{L}}_1^{H,V}\right\}^t \\ \left\{\tilde{\mathbf{L}}_2^{H,V}\right\}^t & -\left\{\tilde{\mathbf{L}}_1^{H,V}\right\}^t \end{pmatrix}. \tag{62}$$

Comparing the expressions (61) and (62) we can observe that for power-flux normalized eigenvector systems, we can use the transpose of a submatrix as the inverse of the other submatrix, via

$$\left\{\tilde{\mathbf{L}}_1^{H,V}(\kappa, x_3, \omega)\right\}^{-1} = 2\left\{\tilde{\mathbf{L}}_2^{H,V}(\kappa, x_3, \omega)\right\}^t \tag{63}$$

$$\left\{\tilde{\mathbf{L}}_2^{H,V}(\kappa, x_3, \omega)\right\}^{-1} = 2\left\{\tilde{\mathbf{L}}_1^{H,V}(\kappa, x_3, \omega)\right\}^t. \tag{64}$$

2.2.2 Deriving alternative power-flux normalized eigenvector sets

We now show how we can derive alternative eigenvector sets directly from the system matrices $\tilde{\mathbf{A}}^H$ and $\tilde{\mathbf{A}}^V$, eqs (21) and (30), respectively. Thereby, we construct our eigenvector matrices in such a way that the eigenvector matrices get the correct shape when the coupling coefficient $\hat{\mathcal{L}} = 0$. For the eigenvector matrices, this means that the rows corresponding to, for example, an electromagnetic field quantity in $\tilde{\mathbf{q}}^V$, should automatically obtain zero elements in their columns corresponding to the mechanical wave types when $\hat{\mathcal{L}}$ is equal to zero.

Let us start by looking at eqs (21), (30), (35), and (36). We can observe that the following relations hold between the system submatrices, the composition and decomposition submatrices and the eigenvalues submatrices

$$\tilde{\mathbf{A}}_{12}^{H,V} = -\tilde{\mathbf{L}}_1^{H,V}\tilde{\boldsymbol{\Lambda}}^{H,V}\left\{\tilde{\mathbf{L}}_2^{H,V}\right\}^{-1} \tag{65}$$

$$\tilde{\mathbf{A}}_{21}^{H,V} = -\tilde{\mathbf{L}}_2^{H,V}\tilde{\boldsymbol{\Lambda}}^{H,V}\left\{\tilde{\mathbf{L}}_1^{H,V}\right\}^{-1} \tag{66}$$

with the eigenvalue submatrices for the SH-TE and P-SV-TM modes described by eqs (37) and (38), respectively. Let us now focus on the specific choices made in deriving the SH-TE and P-SV-TM eigenvector sets. Please note that we follow slightly different procedures while deriving the eigenvectors for both propagation modes. We could, for example, apply the same steps for the SH-TE mode as we describe for the P-SV-TM mode. However, from experience we have noticed that the end-result of this procedure yields numerically less stable results for the SH-TE mode than the alternative way of deriving described here. Vice versa, we cannot apply the SH-TE procedure when deriving the P-SV-TM mode since the size of the system is way bigger and in addition the system is more complicated, making the derivations tedious. On the contrary, the P-SV-TM procedure described here is more straightforward and less tedious, plus it yields numerically stable results for this propagation mode.

2.2.2.1 SH-TE propagation mode
Let us start by focusing on the SH-TE system. We start by rewriting eq. (65) to find an expression for $\tilde{\mathbf{L}}_2^H$ as

$$\tilde{\mathbf{L}}_2^H = -\left\{\tilde{\mathbf{A}}_{12}^H\right\}^{-1}\tilde{\mathbf{L}}_1^H\tilde{\boldsymbol{\Lambda}}^H. \tag{67}$$

We can easily find the inverse of $\tilde{\mathbf{A}}_{12}^H$ since this is a diagonal matrix. We choose $\tilde{\mathbf{L}}_1^H$ in such a way that we obtain the desired structure for $\hat{\mathcal{L}} = 0$ as well as fulfil the physics of the seismo-electromagnetic system. Writing eq. (67) in explicit matrix notation yields

$$\tilde{\mathbf{L}}_2^H = \begin{pmatrix} -\frac{1}{\beta} & 0 \\ 0 & -\frac{1}{\zeta} \end{pmatrix}\begin{pmatrix} d_1^H & d_2^H\chi \\ d_1^H A\chi & d_2^H B \end{pmatrix}\begin{pmatrix} \Gamma_{\text{SH}} & 0 \\ 0 & \Gamma_{\text{TE}} \end{pmatrix} = -\begin{pmatrix} \frac{d_1^H\Gamma_{\text{SH}}}{\beta} & \frac{d_2^H\chi\Gamma_{\text{TE}}}{\beta} \\ -\frac{d_1^H A\chi\Gamma_{\text{SH}}}{\zeta} & -\frac{d_2^H B\Gamma_{\text{TE}}}{\zeta} \end{pmatrix}. \tag{68}$$

Now using eq. (66), we can obtain four equations for solving for two unknowns (A and B).

$$\left(\alpha + \frac{\kappa^2}{\beta}\right)d_1^H + d_1^H A\chi^2 = \frac{d_1^H\Gamma_{\text{SH}}^2}{\beta} \tag{69}$$

$$\left(\alpha + \frac{\kappa^2}{\beta}\right)d_2^H\chi + d_2^H B\chi = \frac{d_2^H\chi\Gamma_{\text{TE}}^2}{\beta} \tag{70}$$

$$d_1^H \chi - \left(\eta^E + \frac{\kappa^2}{\zeta} \right) d_1^H A \chi = -\frac{d_1^H A \chi \Gamma_{\mathrm{SH}}^2}{\zeta} \tag{71}$$

$$d_2^H \chi^2 - \left(\eta^E + \frac{\kappa^2}{\zeta} \right) d_2^H B = -\frac{d_2^H B \Gamma_{\mathrm{TE}}^2}{\zeta}. \tag{72}$$

Dividing out the terms that occur both at the left- and right-hand sides (amongst which are the scaling factors d_1^H and d_2^H), isolating the unknowns A and B and using the relations between spherical and radial wavenumbers (eqs (39) and (40)) yields

$$A = \frac{\gamma_{\mathrm{SH}}^2 - \alpha\beta}{\chi^2 \beta} \tag{73}$$

$$B = \frac{\gamma_{\mathrm{TE}}^2 - \alpha\beta}{\beta} \tag{74}$$

$$A = -\frac{\zeta}{\gamma_{\mathrm{SH}}^2 - \eta^E \zeta} \tag{75}$$

$$B = -\frac{\chi^2 \zeta}{\gamma_{\mathrm{TE}}^2 - \eta^E \zeta}. \tag{76}$$

Remember, we want expressions that are stable when no seismo-electromagnetic coupling occurs (i.e. no divisions by $\hat{\mathcal{L}}$ only). Therefore, we use eq. (75) as the expression for A. For B, the selection is ambiguous. We choose eq. (74) as the expression for B. By equating eq. (73) to (75) and (74) to (76), the following interesting relations can be found

$$\left(\gamma_{\mathrm{SH}}^2 - \alpha\beta \right) \left(\gamma_{\mathrm{SH}}^2 - \eta^E \zeta \right) = -\chi^2 \beta\zeta \tag{77}$$

$$\left(\gamma_{\mathrm{TE}}^2 - \alpha\beta \right) \left(\gamma_{\mathrm{TE}}^2 - \eta^E \zeta \right) = -\chi^2 \beta\zeta. \tag{78}$$

Now that we have solved for the two unknown parameters A and B of the eigenvector matrix, we can normalize the eigenvectors with respect to different quantities. Note that in the whole derivation so far the normalization factors d_1^H and d_2^H dropped out of the equations, meaning that the expressions for the two unknown parameters are normalization independent. Due to the way we have organized our system matrix $\tilde{\mathbf{A}}^H$ (symmetry), and due to the specific structure of the composition matrix $\tilde{\mathbf{L}}^H$ in terms of its submatrices $\tilde{\mathbf{L}}_1^H$ and $\tilde{\mathbf{L}}_2^H$, we can find our power-flux normalization factors, by requiring that

$$\tilde{\mathbf{L}}_1^H \left\{ \tilde{\mathbf{L}}_2^H \right\}^t = \frac{1}{2} \tilde{\mathbf{I}}^H, \tag{79}$$

where we make use of the relations between the transverse and the inverse of certain composition submatrices (eqs 63 and 64).

By requiring eq. (79) to hold we can solve for the flux-normalization scaling factors $d_{1,2}^H$. We combine the expressions for the diagonal elements of $\frac{1}{2}\tilde{\mathbf{I}}^H$ with the expressions for the off-diagonals, yielding expressions containing solely d_1^H or d_2^H. Furthermore, we recognize and apply the relations (77) and (77). Depending on which one of these relations we apply, different end-results for d_1^H and d_2^H are obtained. We choose to use the following end-results as power-flux normalization factors

$$d_1^H = \sqrt{-\frac{\beta \left(\gamma_{\mathrm{SH}}^2 - \eta^E \zeta \right)}{2 \left[\Gamma_{\mathrm{SH}} \left(\gamma_{\mathrm{SH}}^2 - \gamma_{\mathrm{TE}}^2 \right) \right]}} \tag{80}$$

$$d_2^H = \sqrt{-\frac{\beta^2 \zeta}{2 \left[\Gamma_{\mathrm{TE}} \left(\gamma_{\mathrm{SH}}^2 - \gamma_{\mathrm{TE}}^2 \right) \left(\gamma_{\mathrm{TE}}^2 - \alpha\beta \right) \right]}}. \tag{81}$$

We refer to this eigenvector set as the GST SH-TE set.

2.2.2.2 P-SV-TM propagation mode For the P-SV-TM system, we take a slightly different approach, since we cannot find so easily the inverse of $\tilde{\mathbf{A}}_{12}^V$. However, the approach expressed here shows great similarities with the approach presented for the SH-TE mode (and could have also been used for the SH-TE mode). We start by rewriting eq. (66) to find an expression for $\tilde{\mathbf{L}}_2^V$ as

$$\tilde{\mathbf{L}}_2^V = -\tilde{\mathbf{A}}_{21}^V \tilde{\mathbf{L}}_1^V \left\{ \tilde{\mathbf{\Lambda}}^V \right\}^{-1}. \tag{82}$$

Let us now choose $\tilde{\mathbf{L}}_1^V$ in such a way that we obtain the desired structure for $\hat{\mathcal{L}} = 0$ as well as fulfil the physics of the seismo-electromagnetic system. We therefore choose $\tilde{\mathbf{L}}_1^V$ as follows

$$\tilde{\mathbf{L}}_1^V = \begin{pmatrix} d_1^V & d_2^V A & d_3^V B & d_4^V D\chi \\ d_1^V E & d_2^V & d_3^V F & d_4^V G\chi \\ d_1^V N & d_2^V O & d_3^V & d_4^V P\chi \\ 0 & 0 & d_3^V T\chi & d_4^V \end{pmatrix}. \tag{83}$$

As can be observed, we have added the factor χ, containing $\hat{\mathcal{L}}$, to the elements of $\tilde{\mathbf{L}}_1^V$ such that the correct elements of $\tilde{\mathbf{L}}_1^V$ are equal to zero if $\hat{\mathcal{L}}$ equals zero (i.e. that no coupling between the mechanical and electromagnetic parts occurs). What can also be recognized is that two elements (elements (4,1) and (4,2)) are explicitly defined as zero. They correspond to the P-SV-TM mode magnetic field due to the fast and slow compressional waves. As has been shown in various laboratory experiments Bordes *et al.* (2008), the magnetic field is purely associated with shear waves or of course electromagnetic fields. Furthermore, as we see later on when determining the $\tilde{\mathbf{L}}_2^V$ submatrix, these zero elements will move to positions (2,3) and (2,4) in $\tilde{\mathbf{L}}_2^V$, which correspond to the fluid pressure due to SV waves and TM fields. Since the fluid pressure is only associated with the fast and slow pressure waves, these SV and TM elements must be zero, which proves that by choosing the discussed elements equal to zero, the physics of the seismo-electromagnetic phenomenon are correctly preserved. Here, $d_{1:4}^V$ denotes a still to be determined (or chosen) scaling factor that, for example, power flux-normalizes the whole system. Again, $d_{1:4}^V$ can be seen as elements of a diagonal scaling matrix $\tilde{\mathbf{D}}^V$.

As can be observed in eq. (82), we need the inverse of (38) to find $\tilde{\mathbf{L}}_2^V$. This inverse reads

$$\left\{ \tilde{\mathbf{\Lambda}}^V \right\}^{-1} = \begin{pmatrix} \frac{1}{\Gamma_{\text{Pf}}} & 0 & 0 & 0 \\ 0 & \frac{1}{\Gamma_{\text{Ps}}} & 0 & 0 \\ 0 & 0 & \frac{1}{\Gamma_{\text{SV}}} & 0 \\ 0 & 0 & 0 & \frac{1}{\Gamma_{\text{TM}}} \end{pmatrix}. \tag{84}$$

Using eq. (82) we can express $\tilde{\mathbf{L}}_2^V$ in terms of $\tilde{\mathbf{L}}_1^V$ and the known values for the elements of the system submatrix $\tilde{\mathbf{A}}_{21}^V$ and the inverse of the eigenvalues $\{ \tilde{\mathbf{\Lambda}}^V \}^{-1}$, yielding

$$\tilde{\mathbf{L}}_2 = - \begin{pmatrix} \frac{d_1^V}{\Gamma_{\text{Pf}}} \left[s\rho^b + s\rho^f E + j\kappa N \right] & \frac{d_2^V}{\Gamma_{\text{Ps}}} \left[s\rho^b A + s\rho^f + j\kappa O \right] & \frac{d_3^V}{\Gamma_{\text{SV}}} \left[s\rho^b B + s\rho^f F + j\kappa \right] & \frac{d_4^V}{\Gamma_{\text{TM}}} \left[s\rho^b D\chi + s\rho^f G\chi + j\kappa P\chi \right] \\ \frac{d_1^V}{\Gamma_{\text{Pf}}} \left[s\rho^f + s\hat{\rho}^E \left(1 + \frac{\hat{\xi}\hat{\mathcal{L}}}{\varsigma} \right) E \right] & \frac{d_2^V}{\Gamma_{\text{Ps}}} \left[s\rho^f A + s\hat{\rho}^E \left(1 + \frac{\hat{\xi}\hat{\mathcal{L}}}{\varsigma} \right) \right] & 0 & 0 \\ \frac{d_1^V}{\Gamma_{\text{Pf}}} \left[j\kappa + \beta N \right] & \frac{d_2^V}{\Gamma_{\text{Ps}}} \left[j\kappa A + \beta O \right] & \frac{d_3^V}{\Gamma_{\text{SV}}} \left[j\kappa B + \beta \right] & \frac{d_4^V}{\Gamma_{\text{TM}}} \left[j\kappa D\chi + \beta P\chi \right] \\ \frac{d_1^V}{\Gamma_{\text{Pf}}} \left[j\kappa \frac{\hat{\xi}}{\varsigma} E \right] & \frac{d_2^V}{\Gamma_{\text{Ps}}} \left[j\kappa \frac{\hat{\xi}}{\varsigma} \right] & \frac{d_3^V}{\Gamma_{\text{SV}}} \left[j\kappa \frac{\hat{\xi}}{\varsigma} F + \left(-\zeta - \frac{\kappa^2}{\varsigma} \right) T\chi \right] & \frac{d_4^V}{\Gamma_{\text{TM}}} \left[j\kappa \frac{\hat{\xi}}{\varsigma} G\chi + \left(-\zeta - \frac{\kappa^2}{\varsigma} \right) \right] \end{pmatrix}. \tag{85}$$

We can indeed observe that elements (2,3) and (2,4) are zero, as required from a physical point-of-view.

Now that we have defined and consistently determined the composition submatrices $\tilde{\mathbf{L}}_1^V$ and $\tilde{\mathbf{L}}_2^V$ in general terms, respectively, we can use the other equation, eq. (65), to determine a set of equations that contains all necessary information to solve for the unknown parameters of these composition submatrices. To this end, we rewrite eq. (65) as

$$\tilde{\mathbf{A}}_{12}^V \tilde{\mathbf{L}}_2^V = -\tilde{\mathbf{L}}_1^V \tilde{\mathbf{\Lambda}}^V. \tag{86}$$

Writing out eq. (86) explicitly will yield four sets of four equations, one set for each field type (Pf, Ps, SV and TM), which can be used to solve for the unknown parameters. The details of this derivation are presented in the Supporting Information: Appendix G. Solving for the unknown parameters in this way yields

$$N = \frac{-2j\kappa}{\beta} \tag{87}$$

$$E = \frac{\frac{K_c M \hat{\varsigma}}{\hat{c}_{\text{Pf}}^2} - \rho^b M \hat{\varsigma} + \rho^f C \hat{\varsigma}}{M \hat{\varsigma} \rho^f - \hat{\rho}^E C \eta^E} \tag{88}$$

$$A = \frac{-\rho^f M \hat{\varsigma} + \hat{\rho}^E C \eta^E}{\rho^b M \hat{\varsigma} - \rho^f C \hat{\varsigma} - \frac{K_c M \hat{\varsigma}}{\hat{c}_{\text{Ps}}^2}} \tag{89}$$

$$O = NA \tag{90}$$

$$B_1 = s^2 \rho^b - \frac{s^2 \left(\rho^f\right)^2 \hat{\varsigma}}{\hat{\rho}^E \eta^E} - 2 \left(S + G^{fr}\right) \kappa^2 - K_c \gamma_{\mathrm{SV}}^2 \tag{91}$$

$$T_1 = \frac{-2s^3 \kappa^2 \left(\rho^f\right)^2 \hat{\mathcal{L}}^2}{\eta^E B_1} - \frac{\kappa^2}{\hat{\varsigma}} \left(s\hat{\rho}^E \hat{\mathcal{L}}^2 + \eta^E - \hat{\varsigma}\right) + \eta^E \zeta - \gamma_{\mathrm{SV}}^2 \tag{92}$$

$$T = \frac{\frac{-2s\kappa^2 \left(1 + \frac{S}{G^{fr}}\right)}{B_1} - \frac{s}{G^{fr}}}{T_1} \tag{93}$$

$$B = \frac{sj\kappa}{B_1} \left[\frac{\rho^f \hat{\varsigma} \chi T}{\hat{\rho}^E \eta^E} - \left(1 + \frac{S}{G^{fr}}\right) \right] \tag{94}$$

$$F = \frac{-s\rho^f \hat{\varsigma} B - j\kappa \hat{\xi} \chi T}{s\hat{\rho}^E \eta^E} \tag{95}$$

$$D_1 = \left[s^2 \rho^b - \frac{s^2(\rho^f)^2 \hat{\varsigma}}{\hat{\rho}^E \eta^E} - 2 \left(S + G^{fr}\right) \kappa^2 - K_c \gamma_{\mathrm{TM}}^2 \right] \tag{96}$$

$$D_2 = \left[-K_c \left(-\zeta - \frac{\kappa^2}{\hat{\varsigma}}\right) - \frac{S\kappa^2}{\eta^E} - \frac{K_c \xi \chi \kappa^2}{s\rho^f \eta^E \hat{\varsigma}} \right] \tag{97}$$

$$D_3 = \left[s^2 \rho^b S - \frac{s^2 \left(\rho^f\right)^2 S\hat{\varsigma}}{\hat{\rho}^E \eta^E} + 4G^{fr} \left(S + G^{fr}\right) \kappa^2 + s^2 \hat{\rho}^c K_c - \frac{s\rho^f K_c \xi \chi}{\hat{\rho}^E \eta^E} \right] \tag{98}$$

$$P_1 = \left[\frac{s^2 \hat{\rho}^c K_c}{G^{fr}} + 2 \left(S + G^{fr}\right) \kappa^2 - K_c \gamma_{\mathrm{TM}}^2 \right] \tag{99}$$

$$P = \frac{\left[D_1 D_2 + \frac{\kappa^2}{\eta^E} D_3 \right]}{\left[P_1 D_1 + \kappa^2 \left(1 + \frac{S}{G^{fr}}\right) D_3 \right]} \tag{100}$$

$$D = \frac{sj\kappa \left[\frac{1}{\eta^E} - P \left(1 + \frac{S}{G^{fr}}\right) \right]}{D_1} \tag{101}$$

$$G = \frac{-s(\rho^f)^2 \hat{\varsigma} D - j\kappa \hat{\rho}^E}{s\hat{\rho}^E \eta^E \rho^f}. \tag{102}$$

Now that we have solved for all ten unknown parameters of the eigenvector matrix, we can normalize the eigenvectors with respect to different quantities. Note that in the whole derivation so far the normalization factors d_1^V, d_2^V, d_3^V and d_4^V dropped out of the equations, meaning that the expressions for the ten unknown parameters are normalization independent. Where Haartsen & Pride (1997) have used displacement normalization, we here choose for power-flux normalization. Due to the way we have organized our system matrix $\tilde{\mathbf{A}}^V$, and due to the specific structure of the composition matrix $\tilde{\mathbf{L}}^V$ in terms of its submatrices $\tilde{\mathbf{L}}_1^V$ and $\tilde{\mathbf{L}}_2^V$, we can find power-flux normalization factors, by requiring that

$$\{\tilde{\mathbf{L}}_1^V\}^t \, \tilde{\mathbf{L}}_2^V = \frac{1}{2} \tilde{\mathbf{I}}^V, \tag{103}$$

where we make use of the relations between the transverse and the inverse of submatrices (similar to eqs 63 and 64). By requiring eq. (103) to hold and explicitly writing out these submatrix multiplications in general terms, we can solve for the flux-normalization scaling factors $d_{1:4}^V$, yielding

$$d_1^V = \sqrt{-\frac{\Gamma_{\mathrm{Pf}}}{2s \left[\rho^b + E \left(2\rho^f + \frac{\hat{\rho}^E \eta^E E}{\hat{\varsigma}}\right)\right]}} \tag{104}$$

$$d_2^V = \sqrt{-\frac{\Gamma_{\mathrm{Ps}}}{2s \left[A \left(\rho^b A + 2\rho^f\right) + \frac{\hat{\rho}^E \eta^E}{\hat{\varsigma}}\right]}} \tag{105}$$

Table 2. Overview of the velocities, (static) coupling coefficients and porosity values for each of the different media. To illustrate the frequency-dependency of certain wave/field-types, velocity ranges (the real parts of the complex velocities) are displayed for the bandwidth under consideration. Note that the EM-velocities are proportional to the square root of frequency.

Physical quantity	Medium A	Medium B	Medium C	Medium D
Fast P-wave velocity (m s^{-1})	3159.81–3159.84	3153.67–3153.68	3145.83–3145.84	4388.43–4388.43
Slow P-wave velocity (m s^{-1})	2.89–92.96	3.98–131.09	3.92–129.12	3.12–4.25
S-wave velocity (m s^{-1})	2110.79–2110.87	1952.83–1953.03	1959.91–1960.09	1825.74–1825.74
EM-velocity (m s^{-1})	31796.34–1.01×10^6	4496.68–1.42×10^5	4388.31–1.39×10^5	1.00×10^7–2.84×10^7
Coupl. Coeff. (m^2 s V^{-1})	9.07×10^{-9}	2.08×10^{-9}	2.18×10^{-9}	9.07×10^{-14}
Porosity (–)	0.4	0.2	0.21	4×10^{-6}

$$d_3^V = \sqrt{-\frac{\Gamma_{SV}}{2\left[B\left(s\rho^b B + 2j\kappa\right) - \frac{s\hat{\rho}^E\eta^E F^2}{\hat{\varsigma}} + \beta + \Psi\chi^2 T^2\right]}} \tag{106}$$

$$d_4^V = \sqrt{-\frac{\Gamma_{TM}}{2\left[\chi^2\left(s\rho^b D^2 + 2j\kappa P D + \beta P^2\right) - \frac{s\hat{\rho}^E\eta^E\chi^2 G^2}{\hat{\varsigma}} + \Psi\right]}}, \tag{107}$$

with $\Psi = -\zeta - \frac{\kappa^2}{\hat{\varsigma}}$. We have now found expressions for the power-flux normalized eigenvectors of the P-SV-TM system, straight from the system matrices and defined and derived in such a way that they obey the physics of fully decoupled poroelastic and electromagnetic systems when $\hat{\mathcal{L}} = 0$ and remain numerically stable. We refer to this eigenvector set as the GST P-SV-TM set.

3 NUMERICAL EXAMPLES

In this section we present the numerical results of ESSEMOD, using different eigenvector sets. First, we focus on the numerical stability of each of the eigenvector sets. We investigate both the stability and internal consistency of the eigenvector sets using two different tests:

(i) A numerical stability analysis based on the fact that the combination of system matrix, eigenvectors and eigenvalues should yield a zero result.

(ii) A numerical stability test of the flux-normalized eigenvector systems by investigating the preciseness and correctness of using the transpose of the submatrices as its inverse.

We use $Nt = 2048$ time-samples with a time-sampling step of $\Delta t = 0.001$ s. We use the same, two-half-space model for all numerical stability tests, consisting of half-space A over half-space B. The relevant model parameters are specified in Table 2. Note that velocity ranges (the real parts of the complex velocities) are displayed in Table 2 for the bandwidth under consideration. We use a Ricker wavelet with a peak frequency of 30 Hz and a peak amplitude of 1×10^9. The source is located at $x_3 = 100$ m and the receivers are placed at $x_3 = 770$ m depth. The subsurface contains one interface, at $x_3 = 1000$ m depth, such that both coseismic / coelectric fields as well as interface response fields (or seismo-electromagnetic conversion) are generated. In the appendices, we present radial wavenumber–radial frequency (κ-ω) images for each submatrix element, corresponding to certain row-column combinations of the consistency and stability checks.

Next, we investigate what impact the different numerical stability has on the modelling results. We start with a validating comparison between the Haartsen & Pride (1997)-based particle velocity normalized eigenvector set (referred to as the 'HP' set), the Haartsen & Pride (1997)-based flux-normalized eigenvector set (referred to as the 'HPF' set) and our flux-normalized eigenvector set (referred to as the 'GST' set) is made. We use the same model as for the numerical stability tests and proof that all eigenvector sets yield similar results for this model under consideration.

We also consider the special case scenario for this model, where the seismo-electromagnetic coupling coefficient $\hat{\mathcal{L}}$ is chosen equal to zero, resulting in a decoupling of the poroelastic and the electromagnetic parts of the seismo-electromagnetic system. In other words, in this case purely poroelastic and purely electromagnetic systems are modelled, without coupling between electromagnetic and mechanical fields. We investigate the differences between the HPF set and the GST set, for both a purely poroelastic wavefield and a purely electromagnetic field.

We finalize by presenting the results for two different models, that demonstrate the true impact of these numerical stability issues, and issues with low coupling coefficients, on the seismo-electromagnetic modelling results.

3.1 Numerical stability

We now test the different eigenvector sets on their numerical stability and consistency. To this end, we carry out two different tests: a system consistency test and a flux-normalization identity test. We display the results of these checks for each individual submatrix element, for all radial wavenumber–frequency combinations in Appendices A–E, where Appendices A–C display the results of the system consistency tests

and Appendices D and E present the results of the flux-normalization identity tests. Theoretically, all plots should present a zero-value. The computations are carried out in double precision with 15-17 significant decimal bits. The results are plotted on a logarithmic scale, running from 10^{-6} to 10^{-22}. We define 10^{-6} as our threshold-value, where values greater than this threshold are considered to be unacceptable errors (not anymore below numerical precision).

3.1.1 System consistency tests

To check the numerical consistency and stability of the seismo-electromagnetic systems under consideration, we investigate a modified version of eq. (35)

$$\tilde{\mathbf{A}}^{H,V} \tilde{\mathbf{L}}^{H,V} - \tilde{\mathbf{L}}^{H,V} \tilde{\mathbf{\Lambda}}_1^{H,V} = 0. \tag{108}$$

Since the system matrix $\tilde{\mathbf{A}}^{H,V}$ is antidiagonal we can carry-out this check per submatrix. This yields two independent equations that can be used to check the system matrix, eigenvector, and eigenvalue interconsistency and accuracy:

$$\tilde{\mathbf{A}}_{12}^{H,V} \tilde{\mathbf{L}}_2^{H,V} + \tilde{\mathbf{L}}_1^{H,V} \tilde{\mathbf{\Lambda}}^{H,V} = 0 \tag{109}$$

$$\tilde{\mathbf{A}}_{21}^{H,V} \tilde{\mathbf{L}}_1^{H,V} + \tilde{\mathbf{L}}_2^{H,V} \tilde{\mathbf{\Lambda}}^{H,V} = 0. \tag{110}$$

The results of eqs (109) and (110) are referred to as H1 and H2 (for the SH-TE system), respectively, and as V1 and V2 (for the P-SV-TM system), respectively.

Let us first focus on the SH-TE system. We can observe that for the GST set (Figs A1 and A2), the diagonal elements (1,1) and (2,2) of the H2 system (Figs A2a and d) have the largest error. However, all deviations from the expected zero-value result are around the acceptable order of 10^{-10}. This means that the observed variations in deviation from zero are displaying the numerical noise levels.

When we look at the results from the HP set (Figs B1 and B2), we observe that H1 element (2,2) (Fig. B1d) and H2 elements (1,1), (1,2) and (2,2) (Figs A2a, A2b, and A2d, respectively) all have values in the order of 10^{-6} or more, where H2 elements (1,2) and (2,2) (Figs A2b and d) show values in the order of 10^4 and 10^3, respectively.

When we then look at the flux-normalized version of this eigenvector set, HPF (Figs C1 and C2), we can clearly see that the values have decreased significantly. Except H2 element (1,2) (Fig. C2b), which shows a value in the order of 10^{-7}, all elements have values of 10^{-10} or smaller. The way the eigenvectors are normalized plays an important role in the numerical precision and stability of modelling seismo-electromagnetic phenomena. The GST eigenvector set is shown to perform numerically stable for all elements.

Next, we take a closer look at the numerical consistency of the P-SV-TM system. Again, we start by looking at the results of the GST set, displayed in Figs A3 and A4. Most of the elements of both the V1 and V2 systems show values in the order of the numerical noise levels. There is only one visible outlier: V1 element (4,3) (Fig. A3o) with a value in the order of 10^{-8}, but it is still below the threshold of 10^{-6}. This error level is mainly caused due to 'spikes' that occur at specific wavenumber–frequency combinations (e.g. around $\kappa = 0.3$ m^{-1} at 100 Hz). This is visible as the red 'peak' slope in element (4,3) of Fig. A3(o).

Looking at the results from eigenvector set HP (Figs B3 and B4), we can clearly observe larger errors, in multiple elements: V1 elements (2,4) (Fig. B3h), (3,1)-(3,4) (Figs B3i–l), (4,2) (Fig. B3n) and (4,4) (Fig. B3p) and V2 elements (1,1)–(1,4) (Figs B4a–d), (2,1)–(2,4) (Figs B4c–h), (4,1) (Fig. B4m), (4,3) (Fig. B4o) and (4,4) (Fig. B4p). Some of the elements again show huge deviations from the theoretically expected zero-value, resulting in unacceptable error levels (in the order of 1×10^{-6} or higher).

When flux-normalizing this eigenvector set, resulting in the HPF set, we can again observe a significant improvement in numerical consistency and stability. Now, only 4 elements show a significant error: V1 element (3,4) (Fig. C3l) (order 10^{-8}) and V2 elements (2,1), (2,3) and (2,4) (Figs C4c, g and h). Again, flux-normalizing the eigenvector sets is proven to stabilize the numerical results and improve numerical accuracy. In addition, it is again shown that the GST set overall results in the best numerical stability and precision. The numerical consistency errors of the HP and HPF may have implications on finding small amplitude signals when there are also strong signals in the data. The HP and HPF sets may generate disturbing numerical noise that partially masks the small amplitude events (e.g. interface response fields) that can be correctly modelled with the more stable and precise GST set.

Fig. 1 displays the system consistency results for element (1,2) of the *H*2 system, for the HP, HPF and GST eigenvector sets (corresponding to Figs 1a–c, respectively), for a single frequency of 100 Hz as a function of radial wavenumber. These plots provide clear insight in the numerical variations with different wavenumbers. We can clearly observe that the GST set is numerically consistent for this element, the HP set shows unacceptable error levels and the flux-normalizing this HP set results in slightly better consistency, but still less than the GST set.

3.1.2 Flux-normalization identity tests

Now that we have shown that power flux-normalizing the eigenvector sets improves numerical stability/precision and internal system consistency, we focus with our second test only on the power-flux normalized eigenvector sets HPF and GST. We know that for flux-normalized systems, we can express the inverse of the composition matrix in terms of the transposes of the composition submatrices (see e.g.
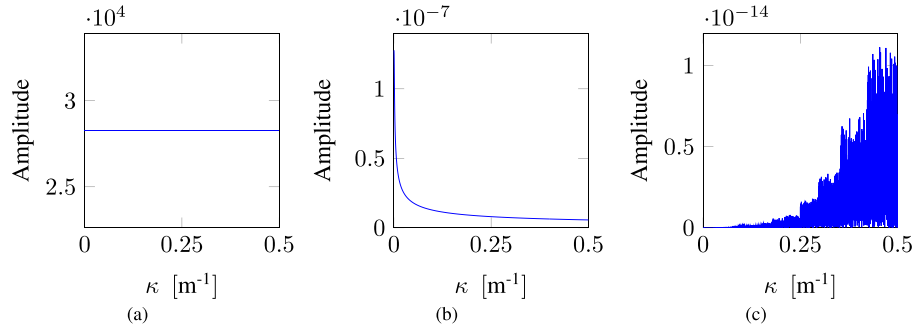
Figure 1. H2 system check, for submatrix element (1,2), plotted for 100 Hz as a function of radial wavenumber κ. (a) HP eigenvector set; (b) HPF eigenvector set; (c) GST eigenvector set.

eq. 62). We make use of this knowledge to carry out the following two numerical checks

$$2\left\{\tilde{\mathbf{L}}_2^{H,V}\right\}^t \tilde{\mathbf{L}}_1^{H,V} - \tilde{\mathbf{I}}^{H,V} = 0 \tag{111}$$

$$2\left\{\tilde{\mathbf{L}}_1^{H,V}\right\}^t \tilde{\mathbf{L}}_2^{H,V} - \tilde{\mathbf{I}}^{H,V} = 0. \tag{112}$$

The results of eq. (111) will be again referred to as H1 and V1 for the SH-TE and P-SV-TM modes, respectively. Similarly, the results of eq. (112) will be referred to as H2 and V2 for the SH-TE and P-SV-TM systems, respectively.

We start again with the SH-TE system. Figs D1 and D2 show that for the GST set, all elements have values less than 10^{-15}, which is beyond numerical precision and hence only displays numerical noise.

For the HPF set, displayed in Figs E1 and E2, we can observe that all elements still show acceptable error levels. However, the maximum values are now in the order of 10^{-10}, slightly higher than the GST set. We can nevertheless conclude that for both flux-normalized eigenvector sets, we can correctly use the transpose of the composition submatrices as an inverse. Another observation is the fact that the matrix of elements of the figures corresponding to H1, Figs D1 and E1, is the transpose of the matrix of elements of the Figs D2 and E2 corresponding to H2, for both the GST and HPF sets.

Let us now look at the P-SV-TM propagation mode. The results for the GST set are presented in Figs D3 and D4. We can observe that most of the elements have values below or around numerical precision. There are a few elements that display slightly higher values: elements (3,4) and (4,3) for V1 (Figs D3l and o) (having values in the order of 10^{-7} and 10^{-8}, respectively) and for V2 the elements (3,4) and (4,3) (Figs D4l and o) (but now having values the other way around; in the order of 10^{-8} and 10^{-7}, respectively). So once again, the figures of V1 and V2 are each other's transpose. The value in the order of 10^{-7} is caused mainly due to the spike around $\kappa = 0.3$ for 100 Hz. In contrast, looking at the results for the HPF set (Figs E3 and E4), we can observe that element (3,4) in V1 (Fig. E3l) and hence (4,3) in V2 (Fig. E4o) have lower values compared to the ones for the GST eigenvector set for these elements. However, other elements, for example, element (1,4) (Fig. E3d) and (2,4) (Fig. E3h) in V1 (and hence (4,1) (Fig. E4m) and (4,2) (Fig. E4n) for V2) display larger values than for the GST set and element (4,3) of V1 (Fig. E3o) and hence (3,4) of V2 (Fig. E4o) for V2 have similar values as the GST set. In conclusion, both flux-normalized eigenvector sets perform also well enough for the P-SV-TM mode when using the transpose of the composition submatrices as an inverse. The GST and HPF sets result in larger and smaller values for different elements. Overall, the GST eigenvector set seems to be slightly more stable for the P-SV-TM mode than the HPF set, but both sets yield acceptable results.

A clear example can be seen in Fig. 2, displaying the flux-normalization identity checks for all radial wavenumbers for a single frequency of 100 Hz. Fig. 2(a) displays the results of the HPF set, Fig. 2(b) of the GST set. We can observe that the GST set results in random deviations
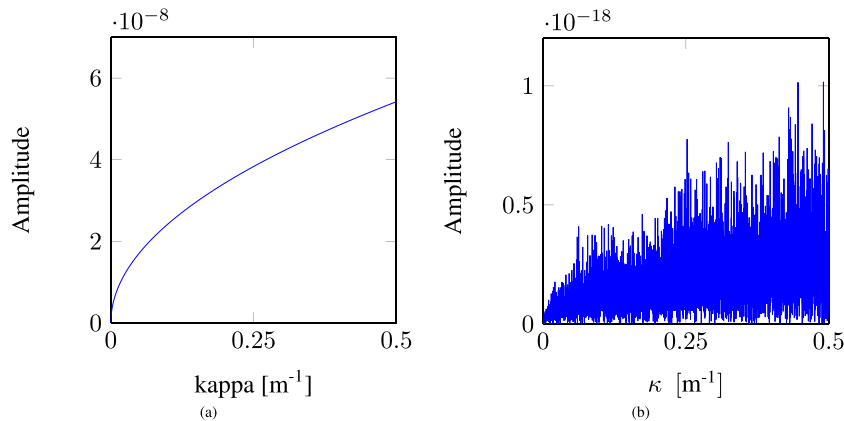
Figure 2. V2 identity check, for submatrix element (4,2), plotted for 100 Hz as a function of radial wavenumber κ. (a) HPF eigenvector set; (b) GST eigenvector set.
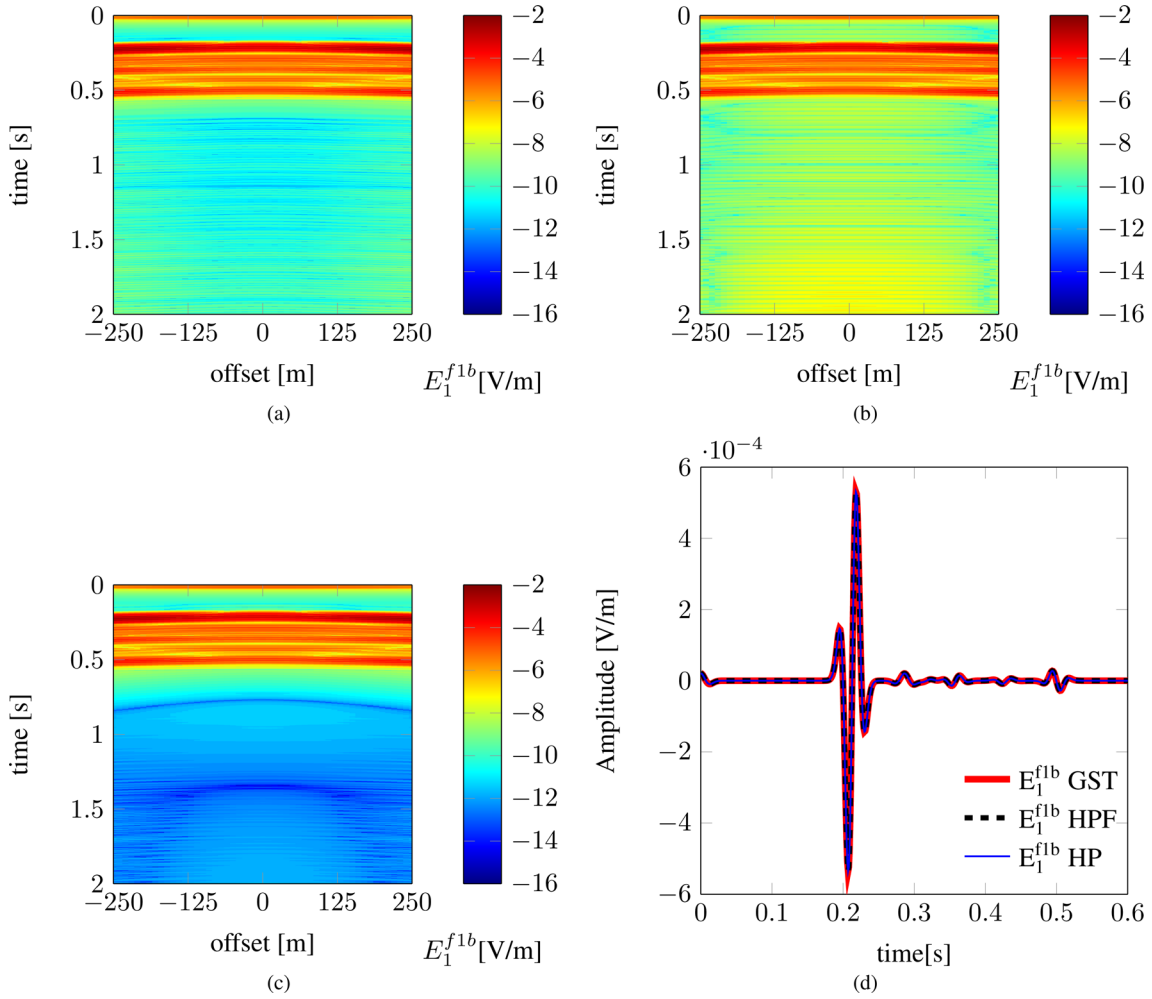
Figure 3. Eigenvector validation comparison of seismo-electromagnetic shot records for a shot at $x_3 = 100$ m depth registered at depth level $x_3 = 770$ m, in a model with an interface at $x_3 = 1000$ m. The displayed fields are the electric field component in the x_1-direction due to a seismic bulk force source component in the same direction. The results of panels (a)–(c) are plotted on a logarithmic scale. (a) seismo-electromagnetic shot records modelled with the HP eigenvector set. (b) Seismo-electromagnetic shot records modelled with the HPF eigenvector set. (c) Seismo-electromagnetic shot records modelled with the GST eigenvector set. (d) Zero-offset trace-overlay of the HPF modelling result displayed with the black-dashed line, the HP result in blue solid and the GST results displayed in red solid.

from zero in the order of 10^{-18}, which is around numerical precision. In contrast, the HPF set shows correlated deviations in the order of 10^{-8}, which might still be acceptable but is obviously numerically less stable and precise.

3.2 Implications for the seismo-electromagnetic modelling results

3.2.1 Validating comparisons between the three eigenvector sets

We here compare the seismo-electromagnetic modelling results of ESSEMOD for an electric field component in the x_1-direction, generated by a seismic dipole bulk force source in the x_1-direction, for the model under consideration. We compare the results of using the HPF set (Fig. 3a), the HP set (Fig. 3b) and the GST set (Fig. 3c). Using the logarithmic plotting scale, we can clearly observe the different seismo-electromagnetic events and we can observe that there is a perfect match between the three eigenvector sets in both phase and amplitude for all events. To illustrate this further, a plot showing a trace-overlay between the HPF set (black-dashed), the HP set (blue-dotted) and the GST set (red solid) is presented in Fig. 3(c). However, differences in the numerical noise levels are visible (e.g. the noise for $t > 0.7$ s). The HP and HPF sets display higher numerical noise levels than the GST eigenvector set. This is an indicator for differences in numerical stability for the different eigenvector sets.

These numerical results serve as a validation for each of the individual eigenvector sets.

### 3.2.2 Numerical inaccuracy: strong and weak events

We have seen that each eigenvector set visibly generates the same results for the two-half-space model under consideration. But what are then the implications of the obvious differences in numerical stability and consistency between the HP, HPF and GST eigenvector sets? To this end, we study a model where an additional second interface is placed 1000 m below the first interface (at a depth of 2000 m) of the numerical consistency model used thus far. The interface separates the upper medium B from the lower medium C, resulting in only a 5 per cent porosity contrast over this interface (and of course a resulting contrast in medium parameters that depend on the porosity). The results are presented in Figs 4 and 5. Looking at Fig. 4, we clearly see that the GST set (Fig. 4c) results in a very clean shot record. The HP set is already less clean (Fig. 4a), and the HPF set shows a lot of numerical noise for the later arrival times (Fig. 4b). We can observe that the strong events arriving roughly in the first 0.5 s are modelled consistently by the HP, HPF and GST sets. However, in Fig. 4(b), we can clearly observe in the HPF results, that the weak events arriving at later times, related mainly to multiple reflections and conversions between the two interfaces, are of similar amplitude as the noise levels. The top inset figure of the trace overlay presented in Fig. 5, clearly shows that after roughly $t = 1$ s, the events modelled with the HPF set (black, dashed) strongly deviate from the GST results (red, solid). These deviations occur for the smaller amplitude events, in this model events with amplitudes in the order of 10^{-7} V m^{-1}. Due to numerical instability, additional wiggles
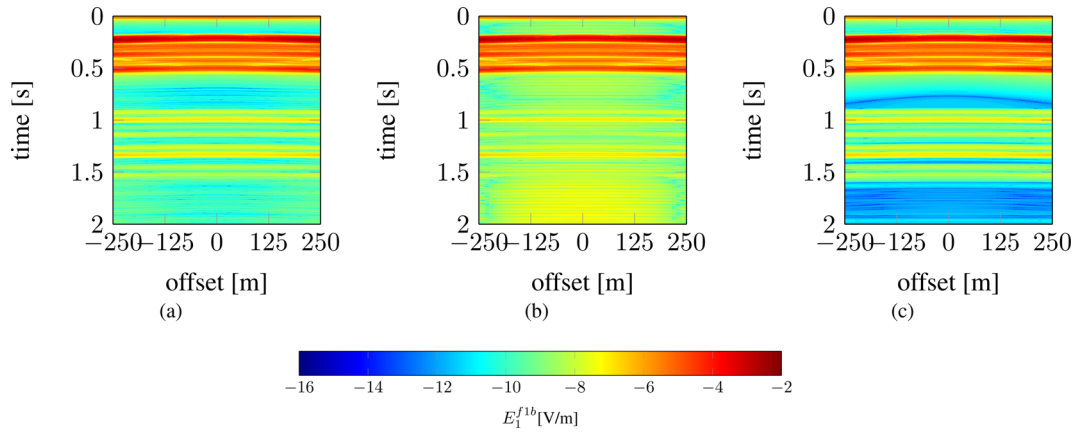
Figure 4. Eigenvector comparison of seismo-electromagnetic shot records for a shot at $x_3 = 100$ m depth registered at depth level $x_3 = 770$ m, in a model with an interface separating medium A from medium B at $x_3 = 1000$ m and an additional interface with only a 5 per cent porosity contrast, separating medium B from medium C, at $x_3 = 2000$ m. The displayed fields are the electric field component in the x_1-direction due to a seismic bulk force source component in the same direction. The results are plotted on a logarithmic scale. (a) Seismo-electromagnetic shot records modelled with the HP eigenvector set. (b) Seismo-electromagnetic shot records modelled with the HPF eigenvector set. (c) Seismo-electromagnetic shot records modelled with the GST eigenvector set.

Figure 5. Zero-offset trace overlay plot of seismo-electromagnetic modelling with three different eigenvector sets. The plots show the results for a shot at $x_3 = 100$ m depth registered at depth level $x_3 = 770$ m, in a model with an interface separating medium A from medium B at $x_3 = 1000$ m and an additional interface with only a 5 per cent porosity contrast, separating medium B from medium C, at $x_3 = 2000$ m. The displayed fields are the electric field component in the x_1-direction due to a seismic bulk force source component in the same direction. The blue-solid line shows the results for the HP set (also the lower zoom inset), the black-dashed line for the HPF set (also the upper zoom inset) and the red-solid line for the GST set.
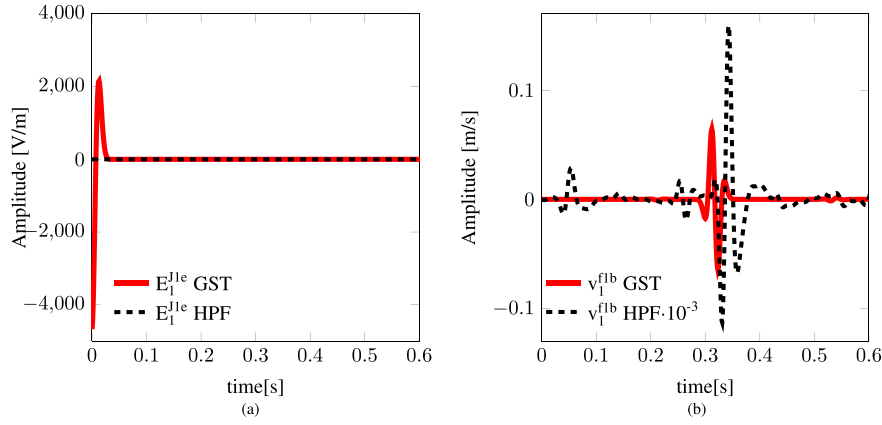
Figure 6. Electric field component in the x_1-direction due to a seismic bulk force source in the same direction, for a shot at $x_3 = 100$ m depth registered at depth level $x_3 = 770$ m in a situation with no seismo-electromagnetic coupling (the coupling coefficient is equal to zero). The results shown are obtained using the GST eigenvector set in red solid, and the HPF set in black-dashed. (a) Zero-offset trace comparison for a purely electromagnetic scenario: the electric field in the x_1-direction due to an electric current source in the same direction. (b) Zero-offset trace comparison for a purely poroelastic scenario: the horizontal particle velocity field component in the x_1-direction due to a dipole bulk force source in the same direction.

are visible, amplitude and waveform differences can be observed, and the noise levels reach values that are similar or even higher than the amplitudes of the events. For the HP eigenvector set (blue, solid), the results match better with the GST set, also for these weaker events at later times in the order of 10^{-7} V m^{-1}. However, for the very weak events in the order of 10^{-10} V m^{-1}, so 3 orders of magnitude weaker, obvious erroneous modelling results can be observed for the HP set (bottom inset figure of Fig. 5), whereas the GST set still models these events numerically stable and clean.

3.2.3 The limiting case of no seismo-electromagnetic coupling

We now investigate the effect of taking $\hat{\mathcal{L}} = 0$ (i.e. no seismo-electromagnetic coupling occurs) on the numerical stability of each eigenvector set. We first explore what happens if we set the seismo-electromagnetic coupling coefficient equal to zero. In other words, we model situations where there is no coupling between poroelastic and electromagnetic fields. In this way, we can model the purely poroelastic and purely electromagnetic fields independently.

We start by focusing on the purely electromagnetic part by looking at the electric field response in the x_1-direction generated by an electric current source in the x_1-direction. Theoretically, we expect only the direct electromagnetic event and its reflection at the interface at depth. Both events will arrive at almost identical times on the seismic time scale (around $t = 0$). The results are presented in Fig. 6(a), a trace overlay for zero-offset. The results of the GST set are presented with the solid red line, and the results using the HPF set are plotted in black-dashed. We can clearly observe that no electromagnetic events are being generated, when using the HPF set, that is, the result is zero whereas we theoretically expect two events. The result of the GST set clearly does show an electromagnetic event around $t = 0$ s. The two expected events show up as one event on a seismic time scale. Similar observations can be made for the other offsets. We have already predicted this behaviour by looking at eqs (F35) and (F36). For additional electromagnetic comparisons of ESSEMOD using the GST eigenvector set with independent electromagnetic modelling codes, the reader is referred to Grobbe *et al.* (2014) and Maas *et al.* (2015).

This electromagnetic test already shows that the HPF set does not correctly model the purely electromagnetic scenario when the coupling coefficient is zero. So how about the purely poroelastic scenario? To answer this question, we look at the results of the x_1-component of the particle velocity generated by a seismic bulk force source in the same direction. Fig. 6(b) shows the zero-offset comparison between the HPF set in black-dashed and the GST set in solid red for this purely poroelastic scenario. The result of the HPF set has been reduced by a factor of 1000. One can clearly see that the HPF set does not model the purely poroelastic scenario correctly either. In contrast, for the results using the GST set we can clearly identify the different events at the correct arrival times that we theoretically expect for this purely poroelastic scenario (direct and reflected fields). Similar observations can be made for the other offsets. To truly validate the correctness in both amplitude and phase, a comparison with an independent poroelastic code can be made. However, for the purpose of this paper, it is sufficient to acknowledge the differences in modelling results between the HPF eigenvector set and the GST eigenvector set in case of decoupled mechanical and electromagnetic fields, recognizing that the GST set correctly models these scenarios whereas the HPF set fails. Do the eigenvector sets yield a correct zero-valued result in case of no seismo-electromagnetic coupling for a seismo-electromagnetic source–receiver combination: the x_1 electric field component generated by a seismic bulk force source in the x_1-direction? Theoretically, this should yield a zero-valued result since no coupling should occur between poroelastic and electromagnetic fields. Comparisons between the HPF set and the GST set indeed showed a zero-valued result at all offsets for both sets (not shown).

We now know that the HPF set (and hence also the HP set) is not correctly modelling the decoupled, purely poroelastic and electromagnetic scenarios when the seismo-electromagnetic coupling coefficient is equal to zero. So, what happens if we model coupled seismo-electromagnetic scenarios in media containing layers with very small coupling coefficients? To this end, we model seismo-electromagnetic phenomena in a
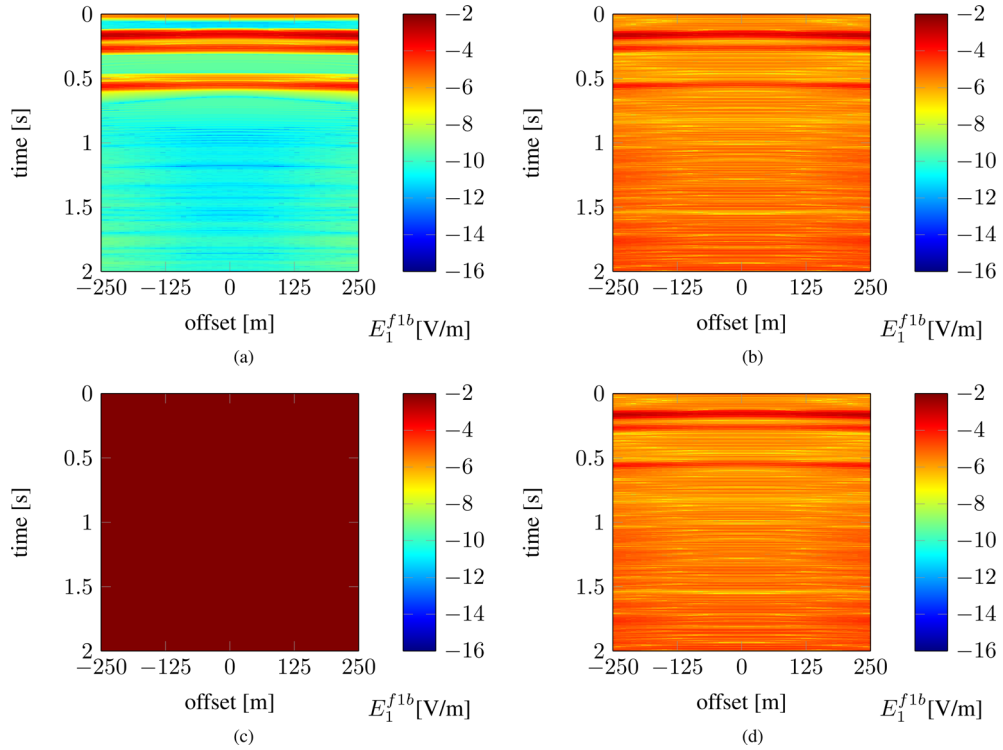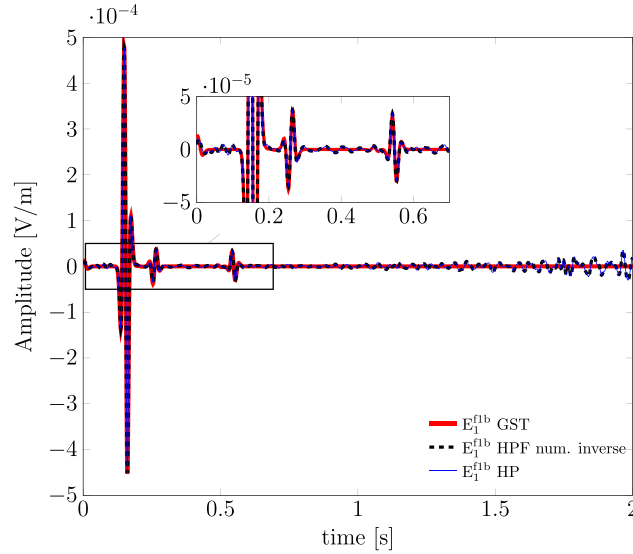
Figure 7. Eigenvector comparison of seismo-electromagnetic shot records for a shot at $x_3 = 100$ m depth registered at depth level $x_3 = 770$ m, in a model with an interface at $x_3 = 1000$ m, separating medium D from medium B. The displayed fields are the electric field component in the x_1-direction due to a seismic bulk force source component in the same direction. The results are plotted on a logarithmic scale. (a) Seismo-electromagnetic shot records modelled with the GST eigenvector set. (b) Seismo-electromagnetic shot records modelled with the HP eigenvector set. (c) Seismo-electromagnetic shot records modelled with the HPF eigenvector set, when the inverse of the eigenvector matrix is obtained from the transposition equivalence property. (d) seismo-electromagnetic shot records modelled with the HPF eigenvector set, when the inverse of the eigenvector matrix is computed numerically.

two half-space model, where the upper half-space (originally medium A) now has a very low porosity (almost approaching a pure solid), and hence a very small coupling coefficient (properties of medium D, see Table 2). The parameters dependent on the porosity of course change accordingly. Figs 7 and 8 show the results of this scenario. In Fig. 7, we can observe that the GST eigenvector set (Fig. 7a) models the seismo-electromagnetic fields correctly and numerically stable. In contrast, the HP eigenvector set fails to correctly model this scenario in a numerically stable fashion (Fig. 7b). Looking at the trace overlay in Fig. 8, we can see that the major events still match reasonably for all three eigenvector sets. However, zooming in to the weaker events in the first 0.7 s, we can observe differences in the amplitude of, for example, the direct source converted EM field at $t = 0$ s. In addition, we can observe that the GST set has very low noise levels (red, solid), whereas the noise levels of the HP set are quite high (blue, solid). As an example, compare the weak amplitude of the arrival around 0.5 s with the noise levels of the HP and HPF sets at earlier and later times (Fig. 8). So for models containing small, multiple arrivals, these arrivals will be masked by the noise levels of the HP set (and the HPF set), and visible in the GST set. Fig. 7(c) shows that the HPF eigenvector set, when exploiting the power flux-normalized transpose property for the inverse, completely fails to model this scenario correctly. However, when the HPF set is used with a numerical inverse instead of making use of this transposition property (eqs 63 and 64), the modelling results are identical to the HP results (compare Figs 7b and d). We can conclude that for modelling scenarios with small coupling coefficients (due to, for example, low porosity values or high electrolyte concentrations), the HP and HPF eigenvector sets can seriously fail to correctly model all the events, especially weaker events (such as certain seismo-electromagnetic interface response fields or multiples). The GST eigenvector set remains stable at all times and always yields clean results.

4 DISCUSSION

The validating results of Fig. 3 have shown that the HP and HPF sets suffer from higher numerical noise levels than the GST set. The HP set shows about 6 orders of magnitude difference between the strongest events in the shot record and the noise levels, the HPF set about 5 orders of magnitude difference and the GST set about 10 orders of magnitude difference. Although this might indicate that the HP set performs slightly better than its flux-normalized HPF version, the numerical stability tests (compare Appendices B and C) have proven that the HPF set overall has better numerical stability and precision than the HP set. The HPF set makes use of the power flux-normalized transpose property to obtain the decomposition matrix (eqs 63 and 64), whereas the HP set was always modelled using a numerical inverse to obtain the decomposition matrix. This numerical inverse probably smooths out numerical inaccuracies and instabilities that can be the consequence of a badly scaled or badly organized composition (eigenvector) matrix, whereas the transposition operation simply reshuffles the values of

Figure 8. Zero-offset trace overlay plot of seismo-electromagnetic modelling with three different eigenvector sets. The plots show the results for a shot at $x_3 = 100$ m registered at depth level $x_3 = 770$ m, in a model with an interface at $x_3 = 1000$ m, separating medium D from medium B. The displayed fields are the electric field component in the x_1-direction due to a seismic bulk force source component in the same direction. The blue-solid line shows the results for the HP set, the black-dashed line for the HPF set, when the inverse of the eigenvector matrix is computed numerically, and the red-solid line for the GST set.

the composition matrix to obtain the decomposition matrix. This fact is nicely illustrated in Fig. 7, where the HPF set yields exactly the same results as the HP set when a numerical inverse is used. The results for the GST set in Fig. 3 display a 10-order difference between signal and numerical noise, already providing a first indication that the GST set yields the best numerical stability and precision. In addition, the two-interface model (Figs 4 and 5) and the low-porosity model (Figs 7 and 8) have proven that the GST set yields stable and clean results at all times, whereas the HPF set and the HP set break down.

So what are these numerical instabilities and inaccuracies caused by? The seismo-electromagnetic composition matrices consist of different parameters and their columns represent different field types (the fast P-wave, slow P-wave, SV-wave, TM-field, SH-wave and the TE-field). The wide variety of seismo-electromagnetic medium parameters can have a wide variety in terms of orders of magnitude: the shear modulus has, for example, relatively large values, whereas the permeability has small values. Also, looking at the wave/field velocities, the Biot slow P-wave has much smaller velocity values than the electromagnetic field velocities. These big and small values interact with each other, for example, in the computation of the global reflection coefficients of the layered-Earth numerical algorithm for each interface in the model. The relative magnitude of the variables in the computations can dictate the severity of round-off errors that are introduced. For example, a loss of numerical precision can occur due to the addition of a large number with a small number. We have seen that power flux-normalizing the HP set (leading to the HPF set), visibly improves the numerical consistency of the eigenvector set (compare Appendices B and C). This normalization based on the power of the system adjusts the composition matrix in such a way, that the relative magnitude of the different variables varies less. The GST eigenvector set is designed completely independently, taking the underlying physics explicitly into account. In addition, the GST set is power flux-normalized, balancing the composition matrix even further. Therefore, the relative magnitude of different variables is more consistent, and varies even less. We must note that the final expressions of the GST eigenvector set for the P-SV-TM mode as presented in this paper are more complicated and extensive than the HPF eigenvector set.

As we have shown, the numerical stability differences have obvious implications on finding small amplitude signals when there are also strong signals in the data (Figs 4 and 5). Especially, later arriving, weak events (e.g. multiples and interface response fields) are masked by numerical noise levels of the HP and HPF sets, whereas these events are correctly modelled with the more stable and precise GST set. Furthermore, the fact that the GST set is capable of correctly modelling scenarios with no seismo-electromagnetic coupling at all (i.e. modelling the independent poroelastic and electromagnetic fields) is an additional benefit. It is also an indication that the physics of the HP and HPF sets are not correctly taken into account. In addition, as soon as there is little coupling between the mechanical and electromagnetic fields (e.g. low porosity values or high electrolyte concentration), the modelling results of the GST set compared to the HP and HPF sets, behave differently. Our modelling scenario clearly shows that the GST set remains stable and models all events correctly and clean, whereas the HP and HPF sets show numerical noise levels that are of similar amplitude as the weak events in the data (Figs 7 and 8). This makes distinguishing between noise and physical weak events impossible. The seismo-electromagnetic interface response fields that we are mainly after since those fields can provide us with information at depth, often have very weak amplitudes. We therefore desire that our numerical modelling codes model all events correctly and as clean as possible, enabling better interface response interpretation of our modelling results.

In the model with two interfaces, as well as the model with weak seismo-electromagnetic coupling, we have only changed the porosity values of the medium compared to the model used for the validation of the eigenvector sets (see Table 2). Of course, many other parameters or parameter combinations, as well as model geometries can yield small seismo-electromagnetic coupling coefficients, weak, late arriving events

or big contrasts between large and small amplitude events. Also, in this paper we have only studied the horizontal electric field due to a seismic bulk force source. There are many other seismo-electromagnetic source–receiver combinations. The numerical effects and instabilities of the HP and HPF eigenvector sets might be even more pronounced for other source–receiver combinations, dependent on, for example, the model scenario under consideration. Furthermore, for the seismic frequency bandwidth, the Biot slow wave is actually a diffusive field that decays very rapidly and diffuses at very low velocities. It almost never shows up in the seismo-electromagnetic shot records. However, when studying seismo-electromagnetic phenomena in, for example, the ultrasonic frequency range, the Biot slow wave becomes a propagating wave and can show up in the records. The importance of accurately modelling the Biot slow wave in numerical seismo-electromagnetic simulations was already mentioned by Pride & Garambois (2002). For ultrasonic frequency bandwidths, the numerical instabilities associated with the parts of the eigenvector sets involved in describing the Biot slow wave might become more pronounced, thereby increasing the importance of numerically precise and stable modelling. Typical seismo-electromagnetic laboratory wave propagation experiments (Schakel *et al.* 2011; Smeulders *et al.* 2014; Zhu *et al.* 2000; Zhu & Toksöz 2005) make use of these ultrasonic frequencies due to the small scale of the experiments. Wave-induced fluid flow modelling for laboratory experiments is recently further addressed by Jougnot *et al.* (2013): using numerical simulations of oscillatory compressibility tests coupled to a model for seismo-electromagnetic conversion in the quasi-static approach, they demonstrate that mesoscopic heterogeneities can produce measurable seismo-electromagnetic signals for typical laboratory configurations. Their experiments show that the frequency range, in combination with the size of the heterogeneities under consideration, plays an important role in the signal measurability. As a follow-up on this work, Monachesi *et al.* (2015) use analytical solutions to describe the seismo-electromagnetic response of a sample, either containing a horizontal layer or a horizontal fracture, where the sample is subjected to an oscillatory compressibility test. By studying these analytical solutions, Monachesi *et al.* (2015) have obtained useful insight into the physical processes that contribute to the seismo-electromagnetic response in media containing mesoscopic heterogeneities. Being able to accurately validate physical laboratory experiments using correct, complete, stable and precise numerical modelling is crucial for our further understanding of the seismo-electromagnetic phenomena and the absolute and relative amplitudes that are to be expected from the different seismo-electromagnetic coupling mechanisms.

One can argue how crucial the discussed errors in the modelling of the weak events are for the overall picture. It is true that all three eigenvector sets model the major events correctly. However, the HPF set already models events, that have a magnitude in the order of 10^{-3} weaker than these major events, not correctly anymore (Fig. 5, top inset). The HP set models events that are 10^{-6} weaker than the largest events incorrectly, and these events are masked by the noise levels (Fig. 5, bottom inset). These are serious errors for numerical modelling, and not negligible. Of course it might be difficult to measure these weaker events in field experiments, but with numerical modelling, we desire our results to be complete, correct, clean and numerically stable. The GST set yields such results at all times, and it is therefore strongly recommended to use this newly developed eigenvector set for future layered-Earth seismo-electromagnetic modelling experiments.

5 CONCLUSIONS

We have shown how to effectively flux-normalize the Haartsen & Pride (1997) eigenvector sets (with particle velocity instead of displacement). In addition, we have derived an alternative flux-normalized eigenvector set directly from the system matrices, thereby imposing specific physical conditions that guarantee correct modelling of the independent poroelastic and electromagnetic systems as well, when the seismo-electromagnetic coupling coefficient is equal to zero. Our approach is in principle applicable to any physical wave or field phenomenon that can be captured in the presented system matrix format.

We have carried out two different numerical stability tests: the first test focused on the internal consistency of the system matrix, its eigenvectors and eigenvalues and the second test focused on the stability and preciseness of the flux-normalized systems.

From the first test we conclude that flux-normalizing the eigenvector sets stabilizes the numerical results and improves numerical accuracy, for both the SH-TE and P-SV-TM propagation modes. Flux-normalizing the HP eigenvector set, resulting in the HPF set, drastically improves the numerical stability, but still there are stability issues. Our GST set results overall in the best numerical performance both in terms of stability and preciseness. The HP and HPF sets showed significant numerical consistency errors for specific matrix elements and certain radial wavenumber–frequency combinations.

The second test focused on how well we can express the inverse of the composition matrix in terms of the transposes of the composition submatrices. For the SH-TE mode, the GST eigenvector set results in slightly smaller errors than the HPF eigenvector set. However, both error levels are acceptable. For the P-SV-TM mode, the GST and HPF sets have larger and smaller errors at different elements. Overall, the GST set seems to be slightly more stable for the P-SV-TM mode, but again both eigenvector sets yield acceptable results. We can conclude that for both flux-normalized eigenvector sets, we can correctly use the transpose of the composition submatrices as an inverse.

We have validated the results using the different eigenvector sets in our analytically based, layered-Earth electromagneto-seismic and seismo-electromagnetic modelling code ESSEMOD. From the validating comparisons using a two-half-space model we conclude that each eigenvector set generates identical results for all the major events in the model under consideration. However, the proven differences in numerical stability and precision between the HP, HPF and GST sets play an important role for different scenarios. As we have shown, the differences have obvious implications on finding small amplitude signals when there are also strong signals in the data. Especially, later arriving, weak events (e.g. multiples and interface response fields) are masked by numerical noise levels of the HP and HPF sets, whereas these events are correctly modelled with the more stable and precise GST set.

When the seismo-electromagnetic coupling coefficient is equal to zero (i.e. when there is no coupling between mechanical and electromagnetic fields), it turns out that only the GST set models the purely poroelastic and purely electromagnetic systems correctly. The incorrect modelling of the independent mechanical and electromagnetic fields by the HP and HPF sets has been explained by theoretically looking at the eigenvector sets as well. It is also an indication that the physics of the HP and HPF sets are not correctly taken into account. Our approach of explicitly enforcing the physics in our derivation of the GST eigenvector set results in correctly modelling of the decoupled purely poroelastic and purely electromagnetic scenarios as well.

In addition, we have shown that as soon as there is little coupling between the mechanical and electromagnetic fields (e.g. low porosity values or high electrolyte concentrations), the modelling results of the GST set, compared to the HP and HPF sets, behave differently. Our modelling scenario clearly shows that the GST set remains stable at all times and models all coupled seismo-electromagnetic events correctly and clean, whereas the HP and HPF sets show clearly numerical noise levels that are of similar amplitude as the weak events in the data, making a distinction between noise and physical weak events impossible.

Although it might be difficult to measure these weaker events in actual field experiments, in numerical modelling, we desire our results to be complete, correct, clean and numerically stable to obtain optimal insights in the physics of seismo-electromagnetic phenomena. The GST set is proven to yield such results at all times, and we therefore strongly recommend to use this newly developed eigenvector set for future layered-Earth seismo-electromagnetic modelling experiments.

ACKNOWLEDGEMENTS

REFERENCES

Airy, G.B., 1833. On the phenomena of Newton's rings when formed between two transparent substances of different refractive powers, *London Edinburgh Phil. Mag. J. Sci.,* **2,** 20–30.

Allègre, V., Jouniaux, L., Lehmann, F. & Sailhac, P., 2010. Streaming potential dependence on water-content in Fontainebleau sand, *Geophys. J. Int.,* **182,** 1248–1266.

Bordes, C., Jouniaux, L., Garambois, S., Dietrich, M., Pozzi, J. & Gaffet, S., 2008. Evidence of the theoretically predicted seismo-magnetic conversion, *Geophys. J. Int.,* **174,** 489–504.

Butler, K.E., Don Russell, R., Kepic, A.W. & Maxwell, M., 1996. Measurement of the seismoelectric response from a shallow boundary, *Geophysics,* **61,** 1769–1778.

Dean, T. & Dupuis, J.C., 2011. The vibroelectric method—a new tool for near-surface characterisation and improved seismic data quality, in *73rd EAGE Conference & Exhibition,* Vienna, **I040,** 1–4, doi:10.3997/2214-4609.20149311.

Frasier, C.W., 1970. Discrete time solution of plane P-SV waves in a plane layered medium, *Geophysics,* **35,** 197–219.

Frenkel, J., 1944. On the theory of seismic and seismoelectric phenomena in moist soil, *J. Phys.,* **8,** 230–241.

Fujinawa, Y. & Noda, Y., 2016. Characteristics of seismoelectric wave fields associated with natural microcracks, *Pure appl. Geophys.,* **173,** 255–268.

Fujinawa, Y., Takahashi, K., Noda, Y., Iitaka, H. & Yazaki, S., 2011. Remote detection of the electric field change induced at the seismic wave front from the start of fault rupturing, *Int. J. Geophys.,* **2011,** 1–11, doi:10.1155/2011/752193.

Garambois, S. & Dietrich, M., 2002. Full waveform numerical simulations of seismoelectromagnetic wave conversions in fluid-saturated stratified porous media, *J. geophys. Res.,* **107,** doi:10.1029/2001JB000316.

Grobbe, N., 2016. Coupled elastic waves and electromagnetic fields in layered porous media - theory, modeling, and interferometric synthesis, *PhD thesis,* Delft University of Technology, TU Delft Repository.

Grobbe, N. & Slob, E., 2013. Validation of an electroseismic and seismoelectric modeling code, for layered earth models, by the explicit homogeneous space solutions, *SEG Expanded Abstracts Houston,* pp. 1847–1851, doi:10.1190/segam2013-1208.1.

Grobbe, N. & Slob, E.C., 2016. Seismo-electromagnetic thin-bed responses: natural signal enhancements?, *J. geophys. Res.,* **121,** doi:10.1002/2015JB012381.

Grobbe, N., Thorbecke, J.W. & Slob, E.C., 2012. ESSEMOD—Electroseismic and seismoelectric flux-normalized modeling for horizontally layered, radially symmetric configurations, *Geophysical Research Abstracts EGU 2012,* **14,** 10011.

Grobbe, N., Hunziker, J. & Slob, E., 2014. Seismoelectric wave propagation modeling for typical laboratory configurations: A numerical validation, in *SEG Expanded Abstracts,* Denver, **2014,** doi:10.1190/segam2014-0689.1.

Grobbe, N., Van der Neut, J., Slob, E., Wapenaar, K., Almagro Vidal, C. & Drijkoningen, G., 2016. Unified multi-depth-level field decomposition, *Geophys. Prospect.,* **64,** 361–391.

Haartsen, M. & Pride, S., 1997. Electroseismic waves from point sources in layered media, *J. geophys. Res.,* **102**(B11), 24 745–24 769.

Haines, S.S. & Pride, S.R., 2006. Seismoelectric numerical modeling on a grid, *Geophysics,* **71**(6), N57–N65.

Hu, H. & Gao, Y., 2011. Electromagnetic field generated by a finite fault due to electrokinetic effect, *J. geophys. Res.,* **116,** B08302, doi:10.1029/2010JB007958.

Hu, H., Guan, W. & Harris, J., 2007. Theoretical simulation of electroacoustic borehole logging in a fluid-saturated porous formation, *J. acoust. Soc. Am.,* **122**(1), 135–145.

Jardani, A. & Revil, A., 2015. Seismoelectric couplings in a poroelastic material containing two immiscible fluid phases, *Geophys. J. Int.,* **202,** 850–870.

Jardani, A., Revil, A., Slob, E. & Söllner, W., 2010. Stochastic joint inversion of 2D seismic and seismoelectric signals in linear poroelastic materials, *Geophysics,* **75,** N19–N31.

Jougnot, D., Rubino, J., Rosas Carbajal, M., Linde, N. & Holliger, K., 2013. Seismoelectric effects due to mesoscopic heterogeneities, *Geophys. Res. Lett.,* **40,** 2033–2037.

Jouniaux, L. & Pozzi, J., 1995. Permeability dependence of streaming potential in rocks for various fluid conductivities, *Geophys. Res. Lett.,* **22,** 485–488.

Kennett, B.L.N., 1983. *Seismic Wave Propagation in Stratified Media,* Cambridge Univ. Press.

Maas, P.J., Grobbe, N., Slob, E.C. & Mulder, W.A., 2015. Electromagnetic & seismoelectric sensitivity analysis using resolution functions, in *77th EAGE Conference & Exhibition,* Madrid, pp. 1–4.

Mahardika, H., Revil, A. & Jardani, A., 2012. Waveform joint inversion of seismograms and electrograms for moment tensor characterization of fracking events, *Geophysics,* **77**(5), ID23–ID39.

Monachesi, L., Rubino, J., Rosas Carbajal, M., Jougnot, D., Linde, N., Quintal, B. & Holliger, K., 2015. An analytical study of seismoelectric signals produced by 1-D mesoscopic heterogeneities, *Geophys. J. Int.,* **201,** 329–342.

Pride, S., 1994. Governing equations for the coupled electromagnetics and acoustics of porous media, *Phys. Rev. B,* **50**(21), 15 678–15 696.

Pride, S. & Garambois, S., 2002. The role of Biot slow waves in electroseismic wave phenomena, *J. acoust. Soc. Am.,* **111**(2), 697–706.

Pride, S. & Morgan, F., 1991. Electrokinetic dissipation induced by seismic waves, *Geophysics,* **56,** 914–925.

Pride, S.R. & Haartsen, M.W., 1996. Electroseismic wave properties, *J. acoust. Soc. Am.,* **100,** 1301–1315.

Ren, H., Huang, Q. & Chen, X., 2010. A new numerical technique for simulating the coupled seismic and electromagnetic waves in layered porous media, *Earthq. Sci.,* **23,** 167–176.

Ren, H., Chen, X. & Huang, Q., 2012. Numerical simulation of coseismic electromagnetic fields associated with seismic waves due to finite faulting in porous media, *Geophys. J. Int.,* **188,** 925–944.

Revil, A. & Mahardika, H., 2013. Coupled hydromechanical and electromagnetic disturbances in unsaturated porous materials, *Water Resour. Res.,* **49,** 744–766.

Revil, A., Naudet, V., Nouzaret, J. & Pessel, M., 2003. Principles of electrography applied to self-potential electrokinetic sources and hydrogeological applications, *Water Resour. Res.,* **39,** SBH3-1–SBH3-15.

Revil, A., Jardani, A., Sava, P. & Haas, A., 2015. *The Seismoelectric Method: Theory and Application,* John Wiley & Sons, Ltd.

Sava, P. & Revil, A., 2012. Virtual electrode current injection using seismic focusing and seismoelectric conversion, *Geophys. J. Int.,* **191,** 1205–1209.

Schakel, M. & Smeulders, D., 2010. Seismoelectric reflection and transmission at a fluid/porous medium interface, *J. acoust. Soc. Am.,* **127,** 13–21.

Schakel, M.D., Smeulders, D.M.J., Slob, E.C. & Heller, H.K.J., 2011. Laboratory measurements and theoretical modeling of seismoelectric inter-face response and coseismic wave fields, *J. Appl. Phys.,* **109,** 074903-1–074903-5.

Schoemaker, F.C., Grobbe, N., Schakel, M.D., de Ridder, S.A.L., Slob, E.C. & Smeulders, D.M.J., 2012. Experimental validation of the electrokinetic theory and development of seismoelectric interferometry by cross-correlation, *Int. J. Geophys.,* **2012,** doi:10.1155/2012/514242.

Smeulders, D.M.J., Grobbe, N., Heller, H.K.J. & Schakel, M.D., 2014. Seismoelectric conversion for the detection of porous medium interfaces containing water and oil, *Vadose Zone J.,* **13**(5), 1–7.

Thompson, A.H. & Gist, G.A., 1993. Geophysical applications of electrokinetic conversion, *Leading Edge,* **12,** 1169–1173.

Ursin, B., 1983. Review of elastic and electromagnetic wave propagation in horizontally layered media, *Geophysics,* **48,** 1063–1081.

Wapenaar, K., 1998. Reciprocity properties of one-way propagators, *Geophysics,* **63,** 1795–1798.

Wapenaar, C. & Berkhout, A., 1989. *Elastic Wavefield Extrapolation—Redatuming of Single and Multi-Component Seismic Data,* Elsevier.

Wapenaar, C.P.A. & Grimbergen, J.L.T., 1996. Reciprocity theorems for one-way wavefields, *Geophys. J. Int.,* **127,** 169–177.

Wapenaar, K., Slob, E. & Snieder, R., 2008. Seismic and electromagnetic controlled-source interferometry in dissipative media, *Geophys. Prospect.,* **56,** 419–434.

Warden, S., Garambois, S., Sailhac, P., Jouniaux, L. & Bano, M., 2012. Curvelet-based seismoelectric data processing, *Geophys. J. Int.,* **190,** 1533–1550.

Warden, S., Garambois, S., Jouniaux, L., Brito, D., Sailhac, P. & Bordes, C., 2013. Seismoelectric wave propagation numerical modelling in partially saturated materials, *Geophys. J. Int.,* **194,** 1498–1513.

Woodhouse, J.H., 1974. Surface waves in a laterally varying layered structure, *Geophys. J. R. astr. Soc.,* **37,** 461–490.

Zhu, Z. & Toksöz, M.N., 2005. Seismoelectric and seismomagnetic measurements in fractured borehole models, *Geophysics,* **70,** F45–F51.

Zhu, Z., Haartsen, M.W. & Toksöz, M.N., 2000. Experimental studies of seismoelectric conversions in fluid-saturated porous media, *J. geophys. Res.,* **105,** 28 055–28 064.

Zyserman, F.I., Gauzellino, P.M. & Santos, J.E., 2010. Finite element modeling of SHTE and PSVTM electroseismics, *J. appl. Geophys.,* **72,** 79–91.

SUPPORTING INFORMATION

Additional Supporting Information may be found in the online version of this paper:

APPENDIX F: DETAILS OF THE POWER-FLUX NORMALIZATION PROCEDURE FOR THE SH-TE AND P-SV-TM HP EIGENVECTOR SET
APPENDIX G: DETAILS OF THE ALTERNATIVELY DERIVED POWER-FLUX NORMALIZED P-SV-TM GST EIGENVECTOR SET
(http://gji.oxfordjournals.org/lookup/suppl/doi:10.1093/gji/ggw128/-/DC1)

Please note: Oxford University Press is not responsible for the content or functionality of any supporting materials supplied by the authors. Any queries (other than missing material) should be directed to the corresponding author for the paper.

## APPENDIX A: SYSTEM CONSISTENCY TEST USING GST EIGENVECTORS

This appendix shows the results of the system consistency tests according to eq. (109), for H1 and V1, and eq. (110), for H2 and V2, respectively. These tests were carried out using the GST eigenvector sets.
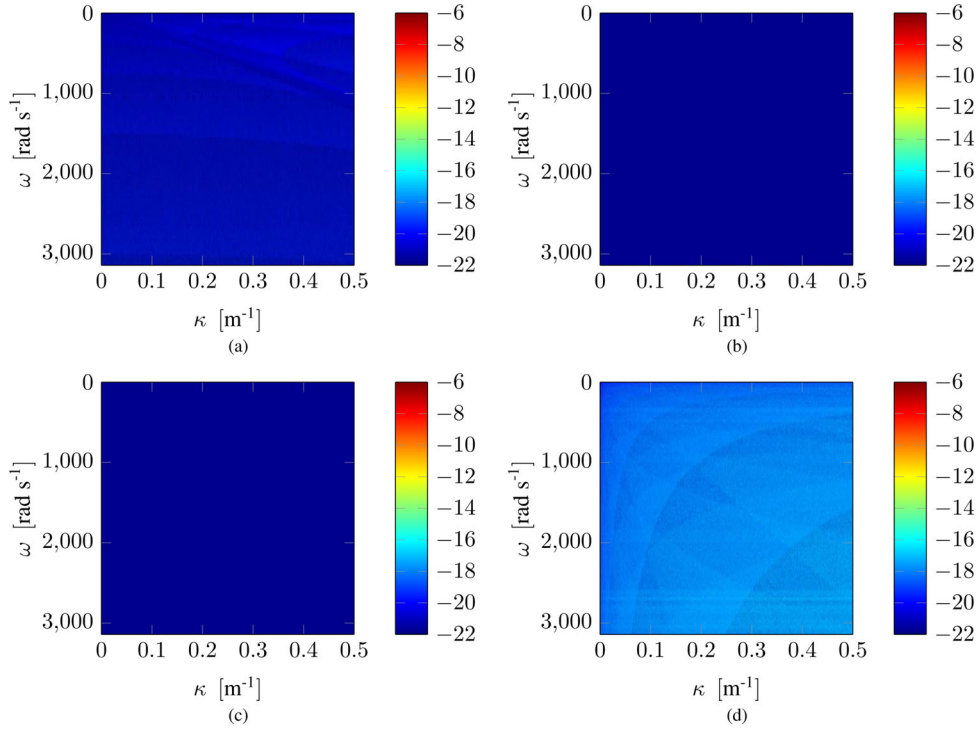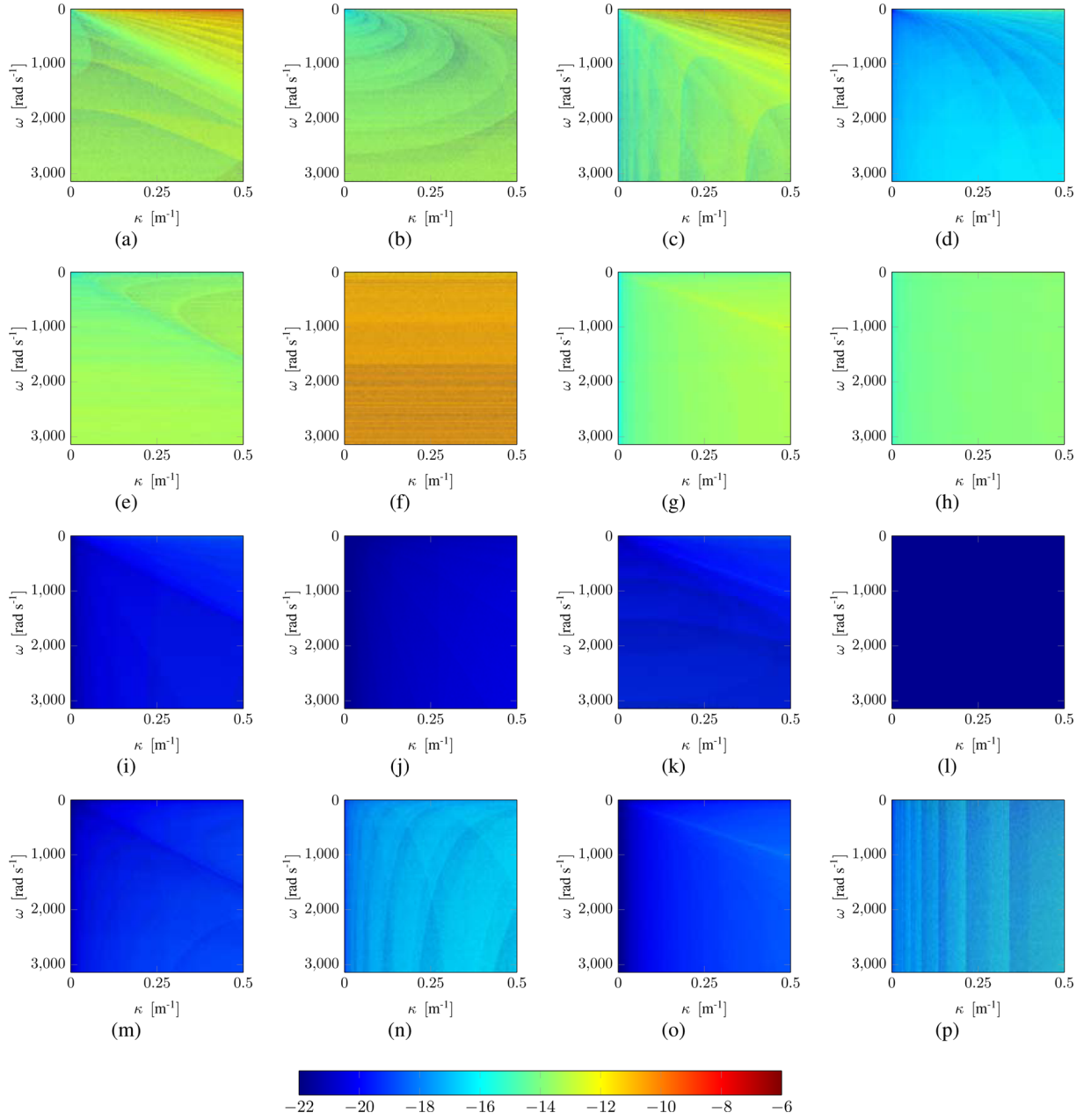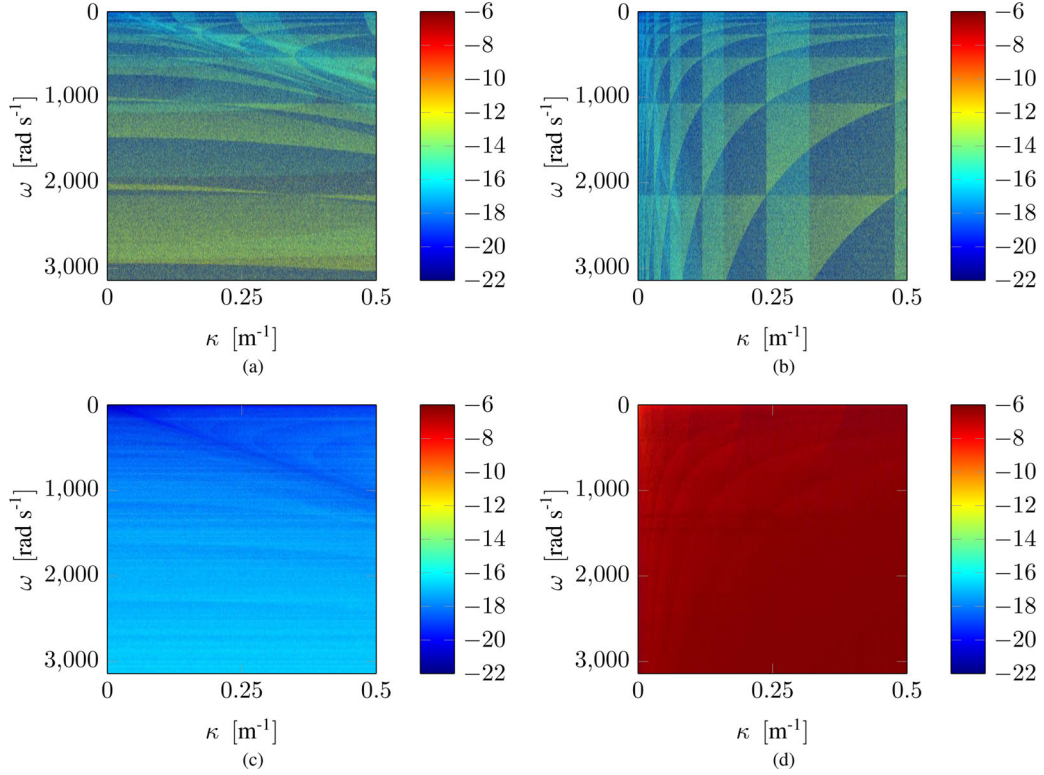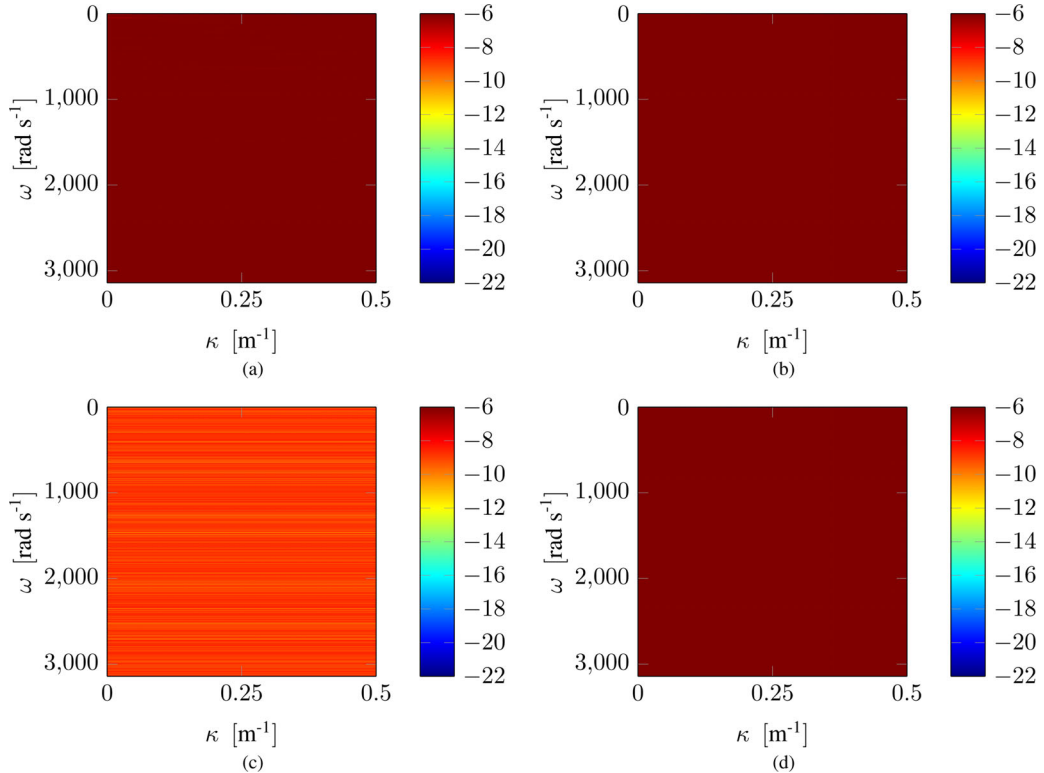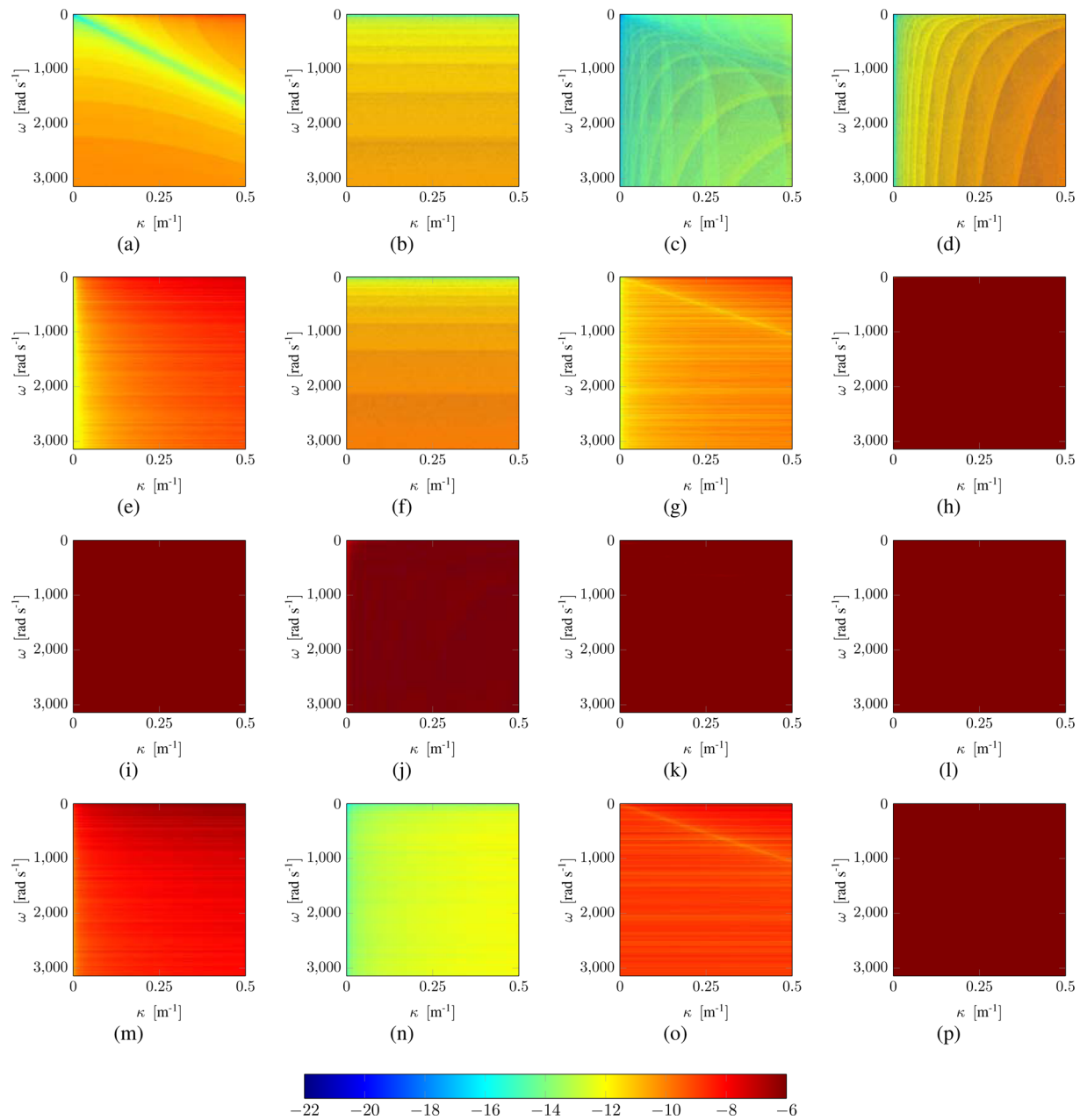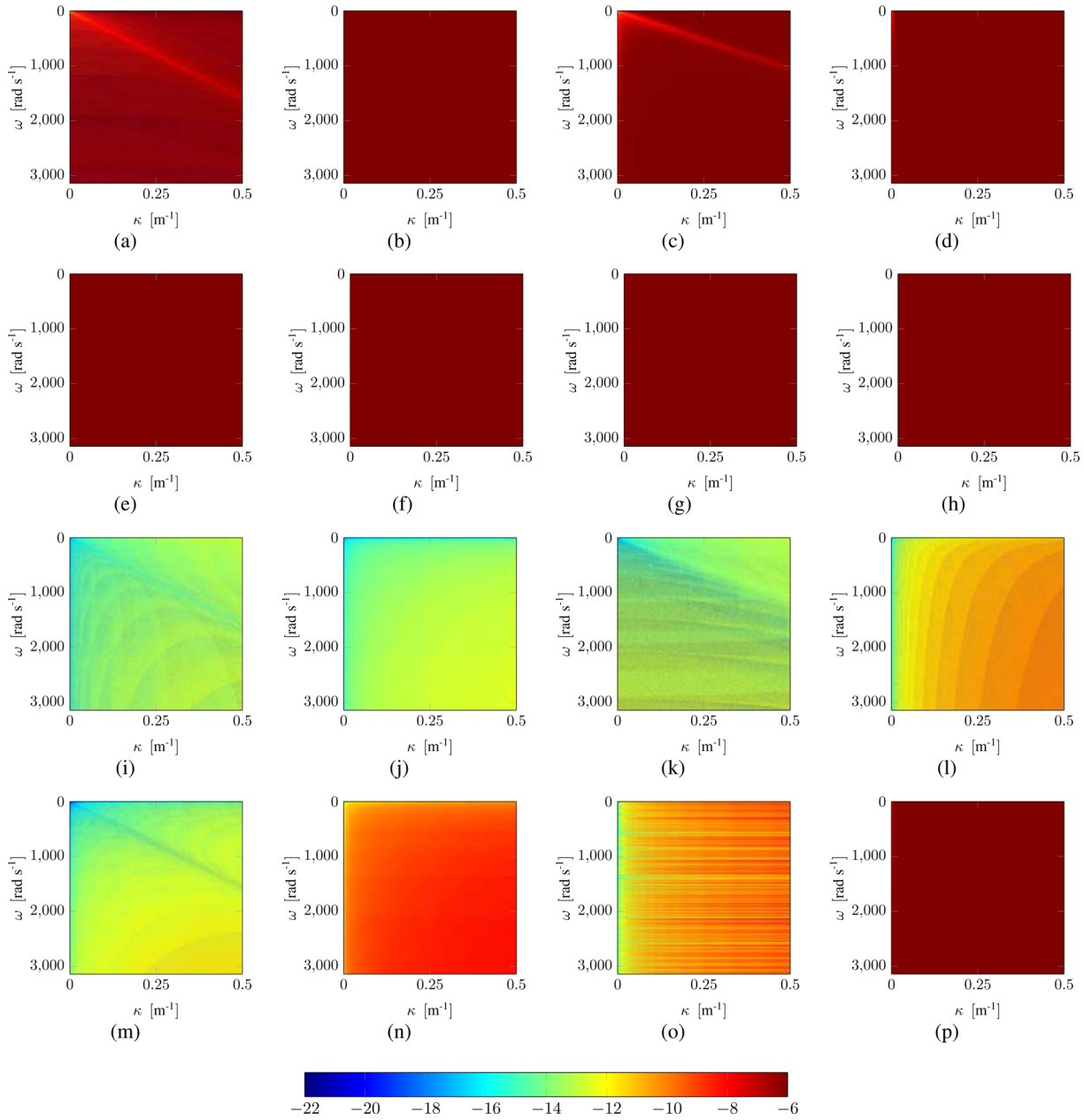

Figure A1. H1 system check with the GST set for all radial wavenumber–angular frequency combinations. (a) Submatrix element (1,1); (b) submatrix element (1,2); (c) submatrix element (2,1); (d) submatrix element (2,2).
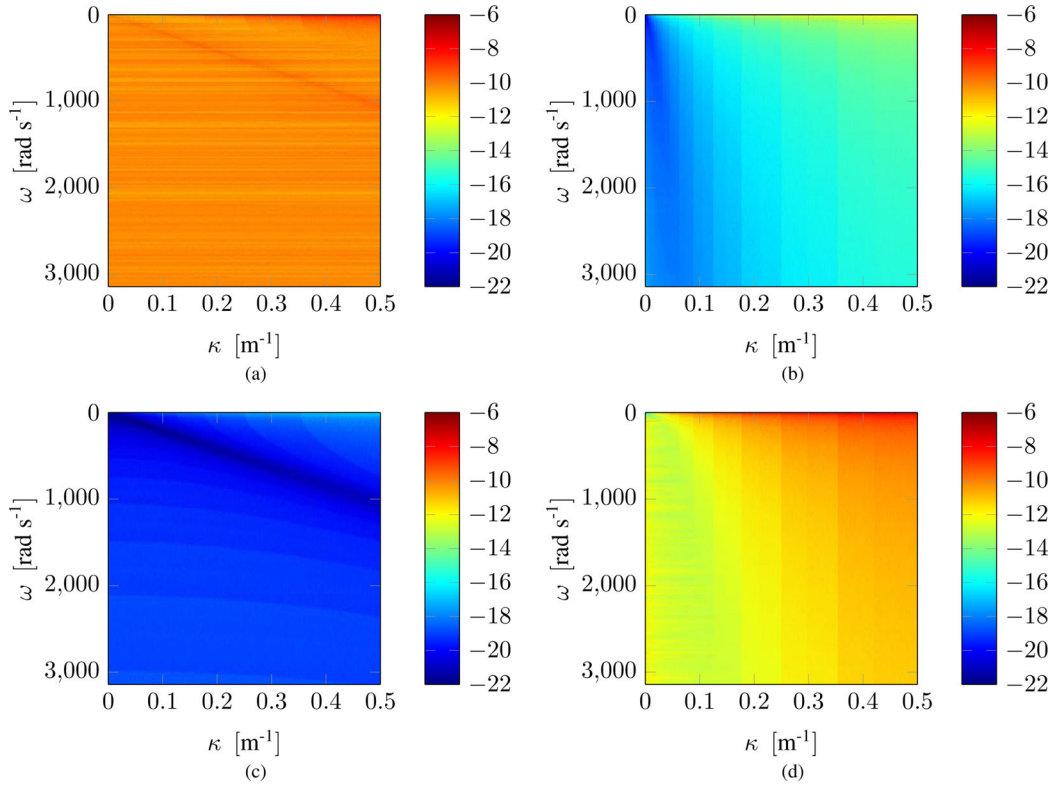
Figure A2. H2 system check with the GST set for all radial wavenumber–angular frequency combinations. (a) Submatrix element (1,1); (b) submatrix element (1,2); (c) submatrix element (2,1); (d) submatrix element (2,2).
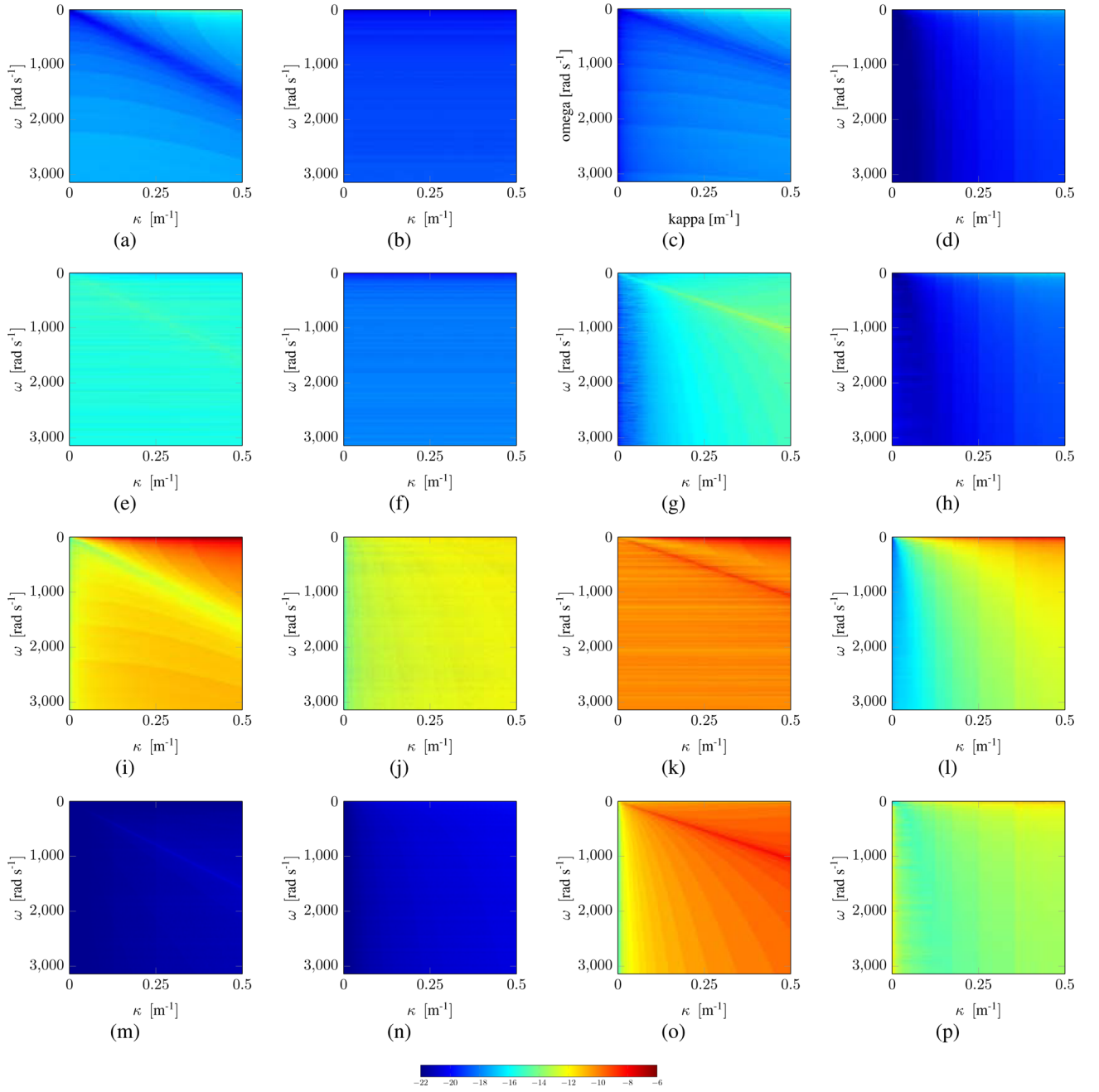
Figure A3. V1 system check with the GST set for all radial wavenumber–angular frequency combinations. (a) Submatrix element (1,1); (b) submatrix element (1,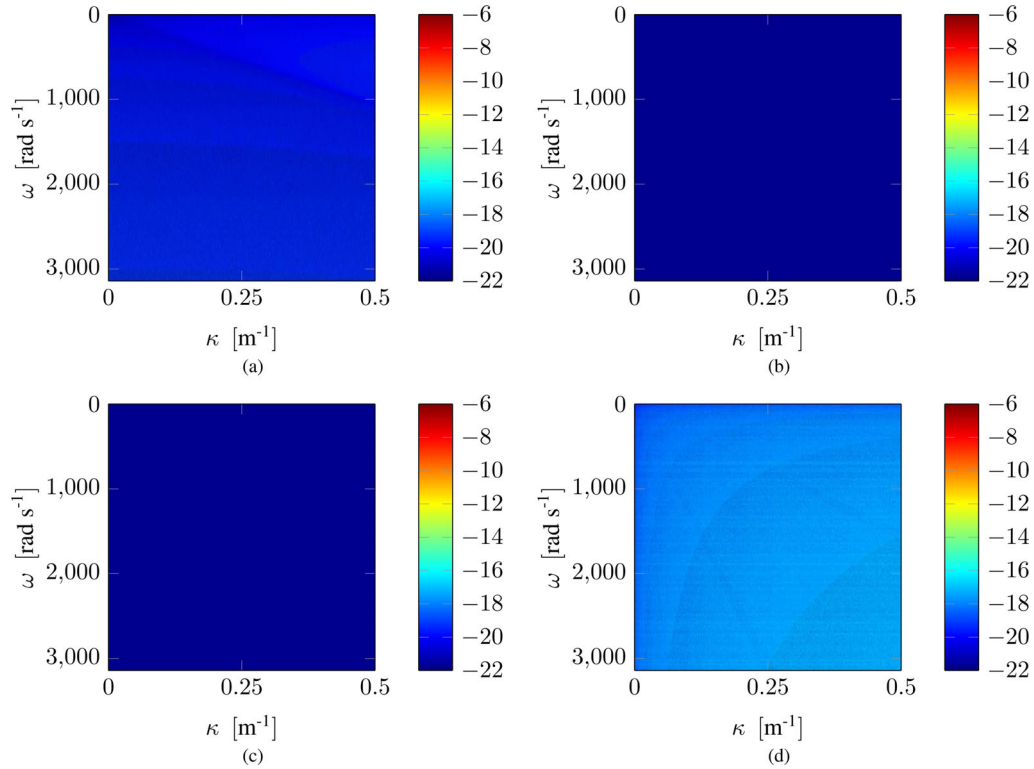2); (c) submatrix element (1,3); (d) submatrix element (1,4); (e) submatrix element (2,1); (f) submatrix element (2,2); (g) submatrix element (2,3); (h) submatrix element (2,4); (i) submatrix element (3,1); (j) submatrix element (3,2); (k) submatrix element (3,3); (l) submatrix element (3,4); (m) submatrix element (4,1); (n) submatrix element (4,2); (o) submatrix element (4,3); (p) submatrix element (4,4).

Figure A4. V2 system check with the GST set for all radial wavenumber–angular frequency combinations. (a) Submatrix element (1,1); (b) submatrix element (1,2); (c) submatrix element (1,3); (d) submatrix element (1,4); (e) submatrix element (2,1); (f) submatrix element (2,2); (g) submatrix element (2,3); (h) submatrix element (2,4); (i) submatrix element (3,1); (j) submatrix element (3,2); (k) submatrix element (3,3); (l) submatrix element (3,4); (m) submatrix element (4,1); (n) submatrix element (4,2); (o) submatrix element (4,3); (p) submatrix element (4,4).

## APPENDIX B: SYSTEM CONSISTENCY TEST USING HP EIGENVECTORS

This appendix shows the results of the system consistency tests according to eq. (109), for H1 and V1, and eq. (110), for H2 and V2, respectively. These tests were carried out using the HP eigenvector sets.

Figure B1. H1 system check with the HP set for all radial wavenumber–angular frequency combinations. (a) Submatrix element (1,1); (b) submatrix element (1,2); (c) submatrix element (2,1); (d) submatrix element (2,2).

Figure B2. H2 system check with the HP set for all radial wavenumber–angular frequency combinations. (a) Submatrix element (1,1); (b) submatrix element (1,2); (c) submatrix element (2,1); (d) submatrix element (2,2).
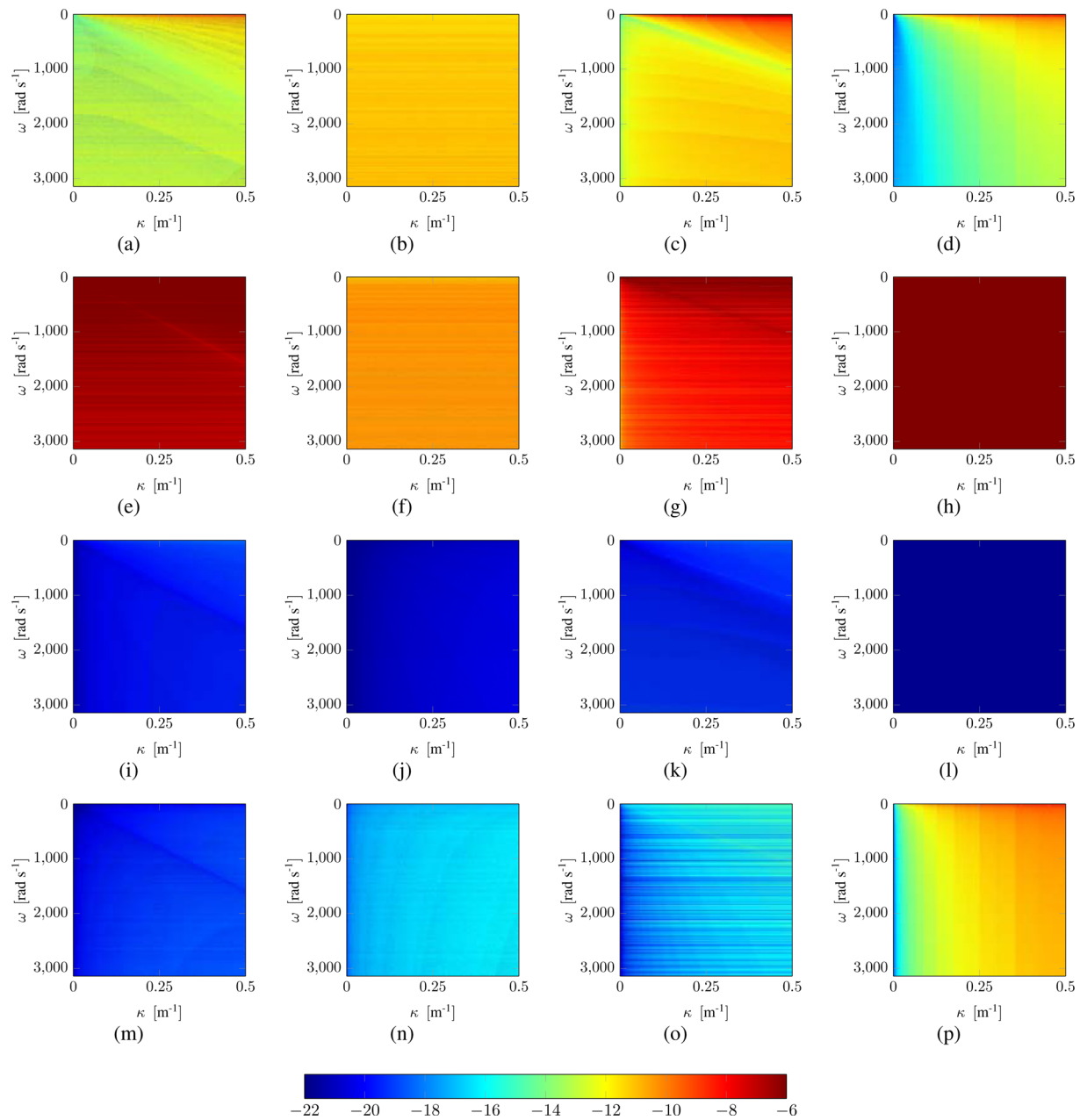
Figure B3. V1 system check with the HP set for all radial wavenumber–angular frequency combinations. (a) Submatrix element (1,1); (b) submatrix element (1,2); (c) submatrix element (1,3); (d) submatrix element (1,4); (e) submatrix element (2,1); (f) submatrix element (2,2); (g) submatrix element (2,3); (h) submatrix element (2,4); (i) submatrix element (3,1); (j) submatrix element (3,2); (k) submatrix element (3,3); (l) submatrix element (3,4); (m) submatrix element (4,1); (n) submatrix element (4,2); (o) submatrix element (4,3); (p) submatrix element (4,4).

Figure B4. V2 system check with the HP set for all radial wavenumber–angular frequency combinations. (a) Submatrix element (1,1); (b) submatrix element (1,2); (c) submatrix element (1,3); (d) submatrix element (1,4); (e) submatrix element (2,1); (f) submatrix element (2,2); (g) submatrix element (2,3); (h) submatrix element (2,4); (i) submatrix element (3,1); (j) submatrix element (3,2); (k) submatrix element (3,3); (l) submatrix element (3,4); (m) submatrix element (4,1); (n) submatrix element (4,2); (o) submatrix element (4,3); (p) submatrix element (4,4).

APPENDIX C: SYSTEM CONSISTENCY TEST USING HPF EIGENVECTORS

This appendix shows the results of the system consistency tests according to eq. (109), for H1 and V1, and eq. (110), for H2 and V2, respectively. These tests were carried out using the HPF eigenvector sets.

Figure C1. H1 system check with the HPF set for all radial wavenumber–angular frequency combinations. (a) Submatrix element (1,1); (b) submatrix element (1,2); (c) submatrix element (2,1); (d) submatrix element (2,2).
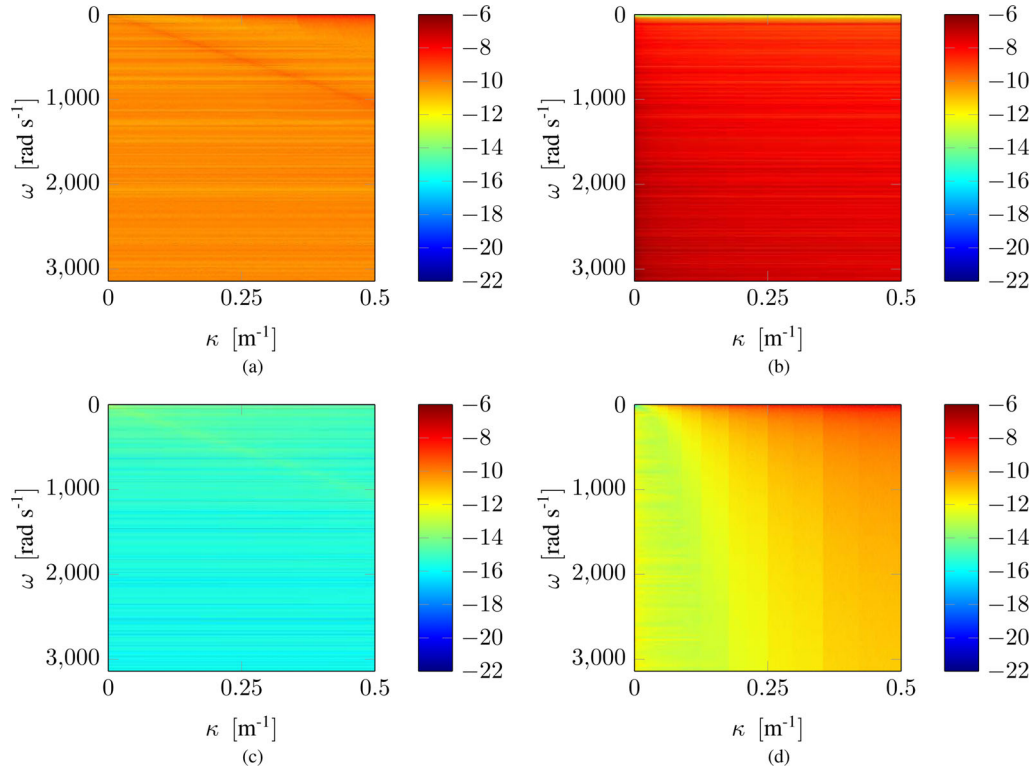
Figure C2. H2 system check with the HPF set for all radial wavenumber–angular frequency combinations. (a) Submatrix element (1,1); (b) submatrix element (1,2); (c) submatrix element (2,1); (d) submatrix element (2,2).
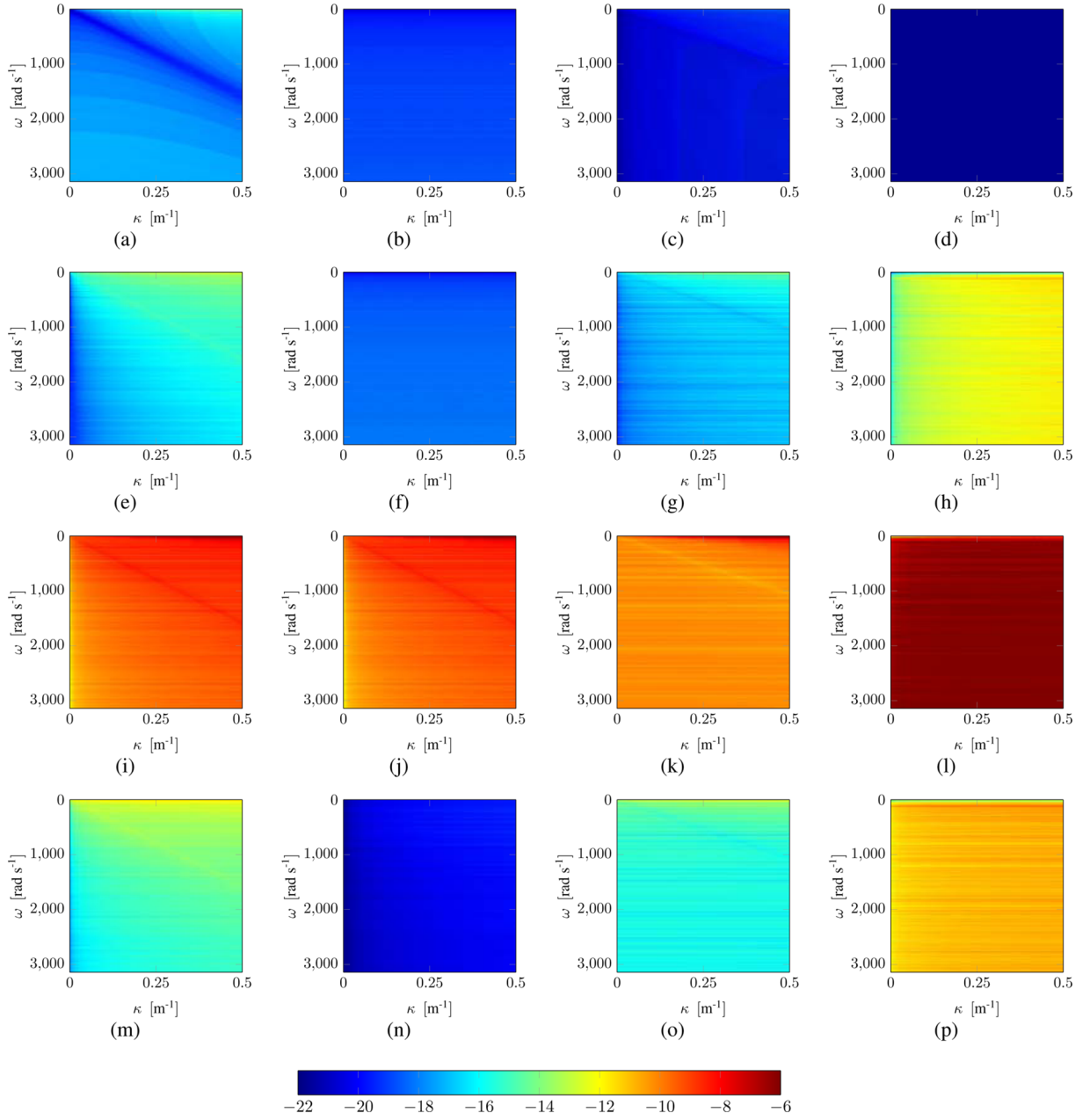
Figure C3. V1 system check with the HPF set for all radial wavenumber–angular frequency combinations. (a) Submatrix element (1,1); (b) submatrix element (1,2); (c) submatrix element (1,3); (d) submatrix element (1,4); (e) submatrix element (2,1); (f) submatrix element (2,2); (g) submatrix element (2,3); (h) submatrix element (2,4); (i) submatrix element (3,1); (j) submatrix element (3,2); (k) submatrix element (3,3); (l) submatrix element (3,4); (m) submatrix element (4,1); (n) submatrix element (4,2); (o) submatrix element (4,3); (p) submatrix element (4,4).
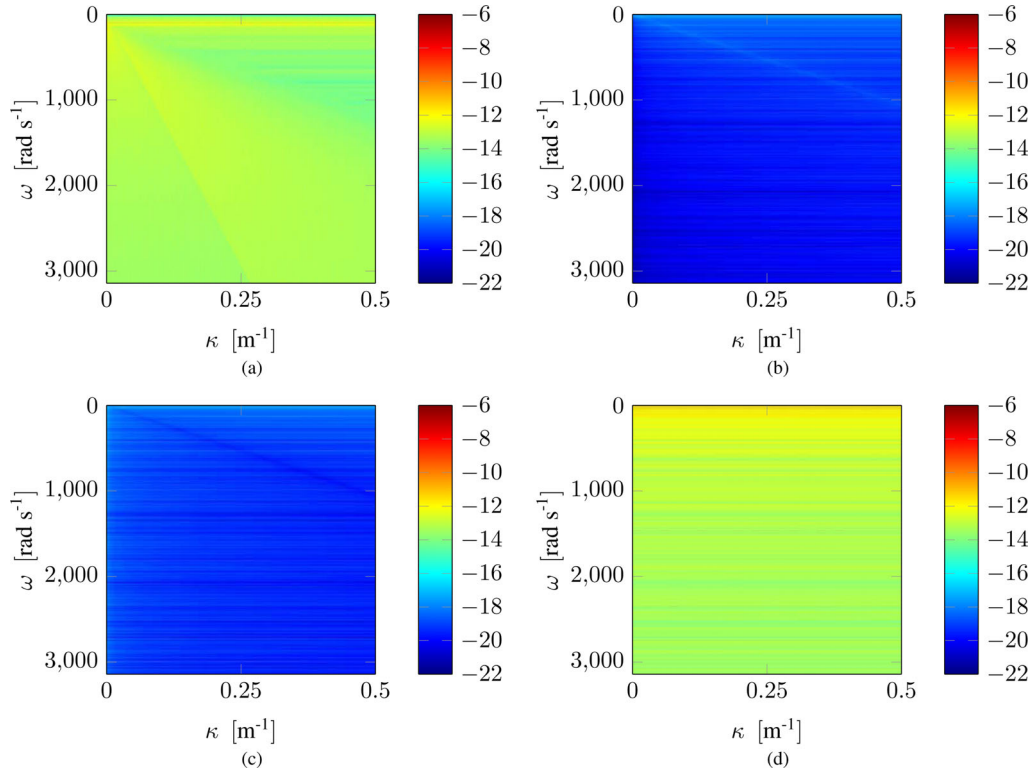
Figure C4. V2 system check with the HPF set for all radial wavenumber–angular frequency combinations. (a) submatrix element (1,1) (b) submatrix element (1,2) (c) submatrix element (1,3) (d) submatrix element (1,4) (e) submatrix element (2,1) (f) submatrix element (2,2) (g) submatrix element (2,3) (h) submatrix element (2,4) (i) submatrix element (3,1) (j) submatrix element (3,2) (k) submatrix element (3,3) (l) submatrix element (3,4) (m) submatrix element (4,1) (n) submatrix element (4,2) (o) submatrix element (4,3) (p) submatrix element (4,4).

APPENDIX D: FLUX-NORMALIZATION IDENTITY TEST USING GST EIGENVECTORS

This appendix shows the results of the flux-normalization identity tests according to eq. (111), for H1 and V1, and eq. (112), for H2 and V2, respectively. These tests were carried out using the GST eigenvector sets.
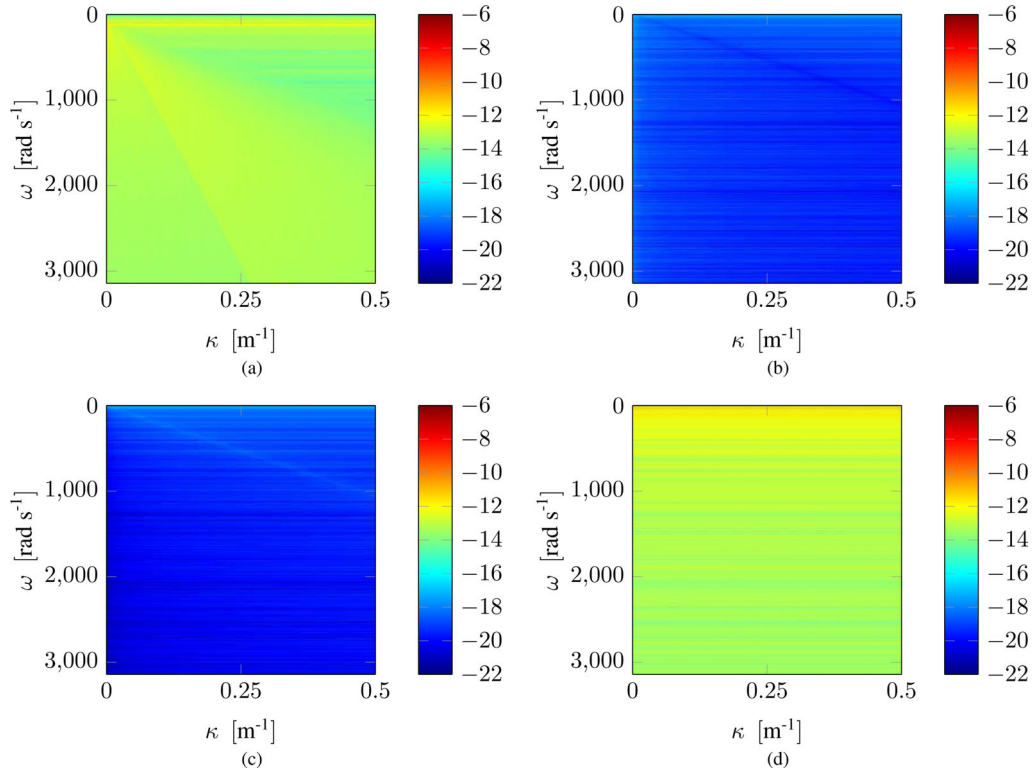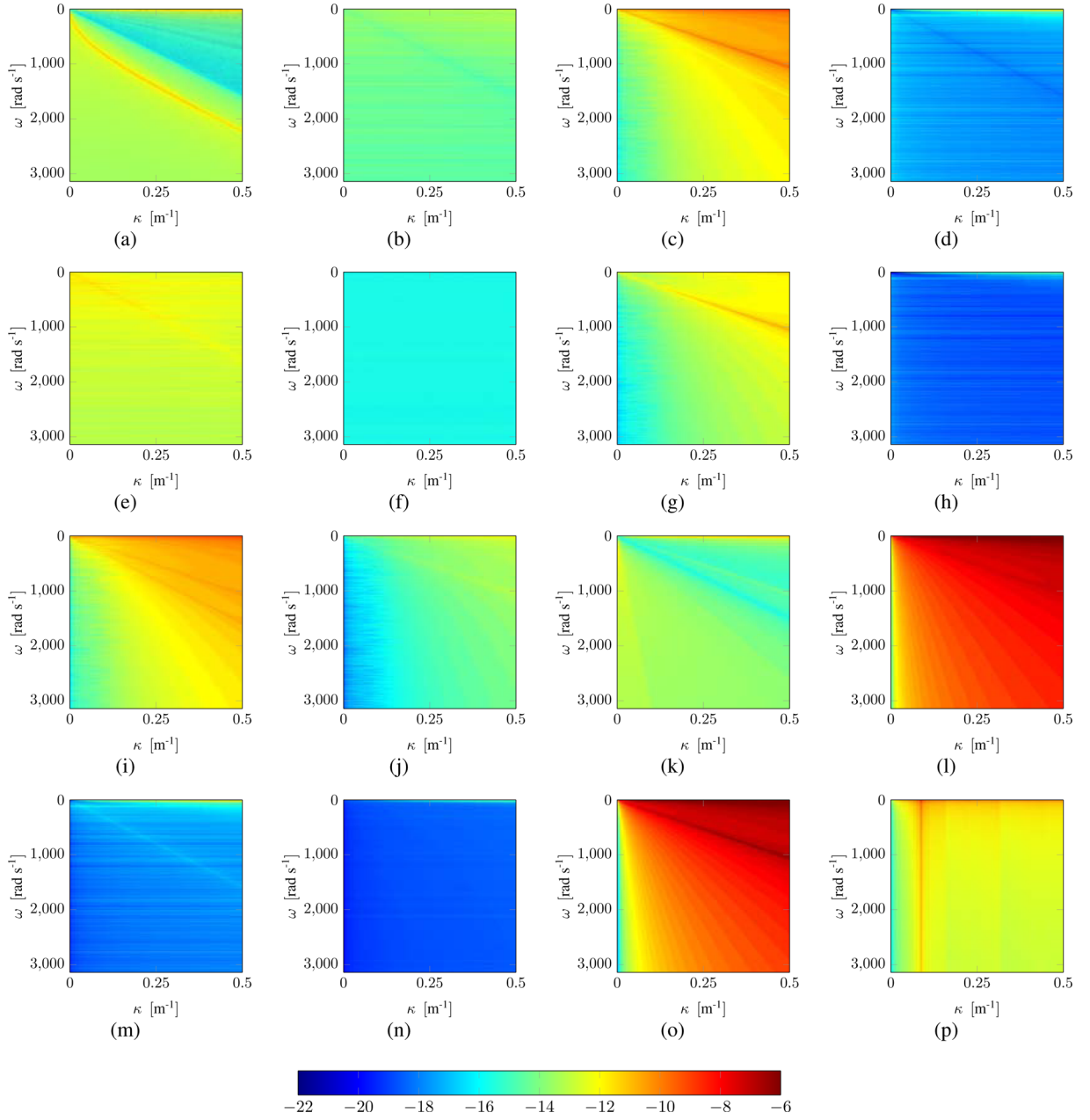

Figure D1. H1 identity check with the GST set for all radial wavenumber–angular frequency combinations. (a) Submatrix element (1,1); (b) submatrix element (1,2); (c) submatrix element (2,1); (d) submatrix element (2,2).

Figure D2. H2 identity check with the GST set for all radial wavenumber–angular frequency combinations. (a) Submatrix element (1,1); (b) submatrix element (1,2); (c) submatrix element (2,1); (d) submatrix element (2,2).
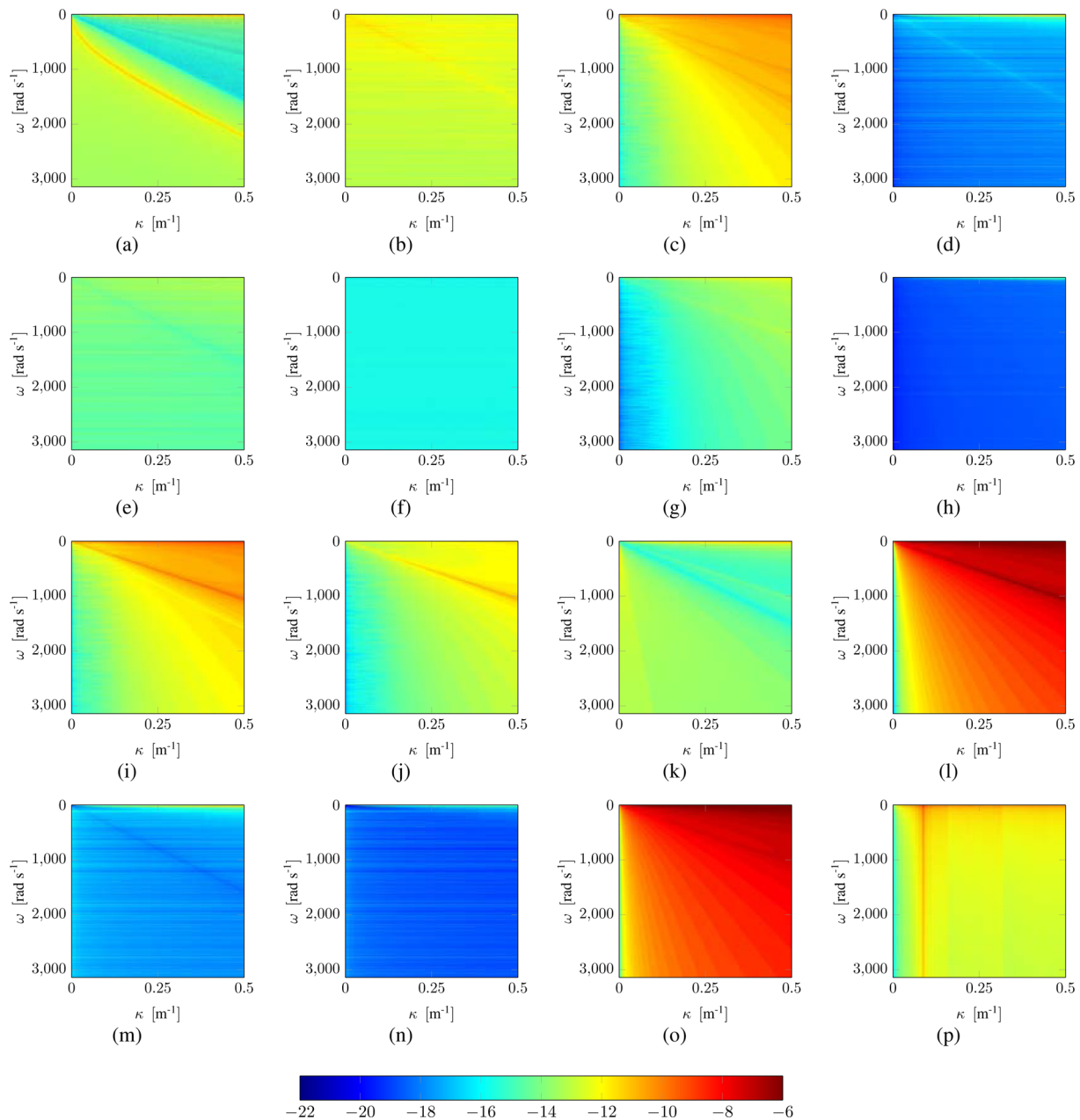
Figure D3. V1 identity check with the GST set for all radial wavenumber–angular frequency combinations. (a) Submatrix element (1,1); (b) submatrix element (1,2); (c) submatrix element (1,3); (d) submatrix element (1,4); (e) submatrix element (2,1); (f) submatrix element (2,2); (g) submatrix element (2,3); (h) submatrix element (2,4); (i) submatrix element (3,1); (j) submatrix element (3,2); (k) submatrix element (3,3); (l) submatrix element (3,4); (m) submatrix element (4,1); (n) submatrix element (4,2); (o) submatrix element (4,3); (p) submatrix element (4,4).
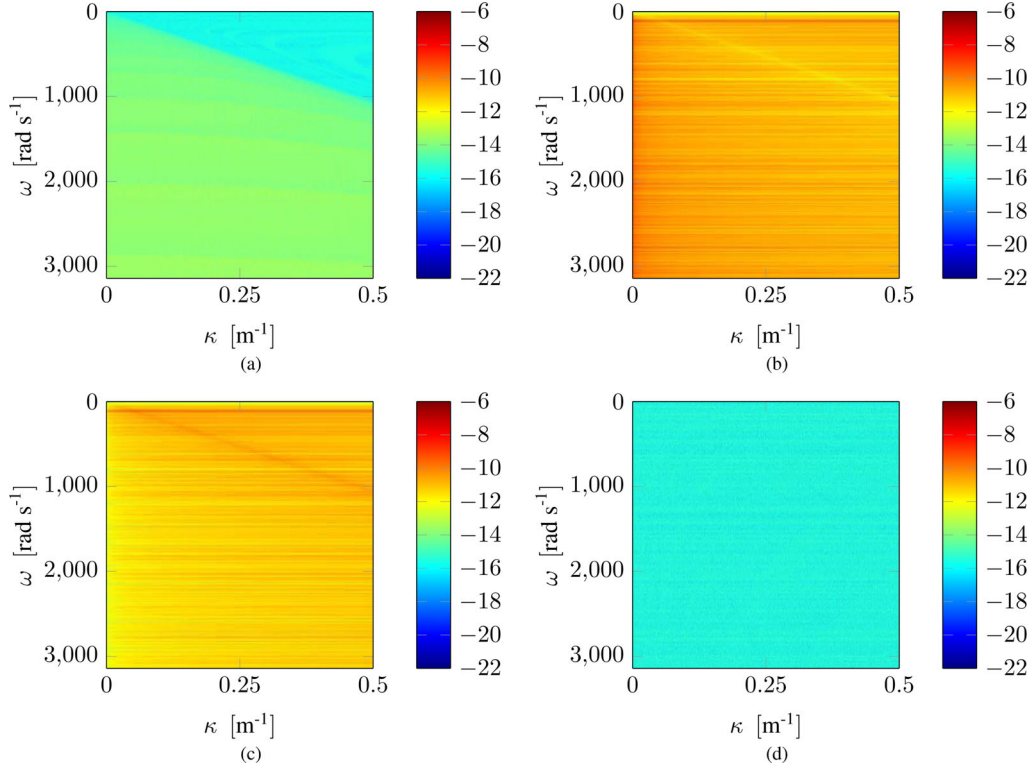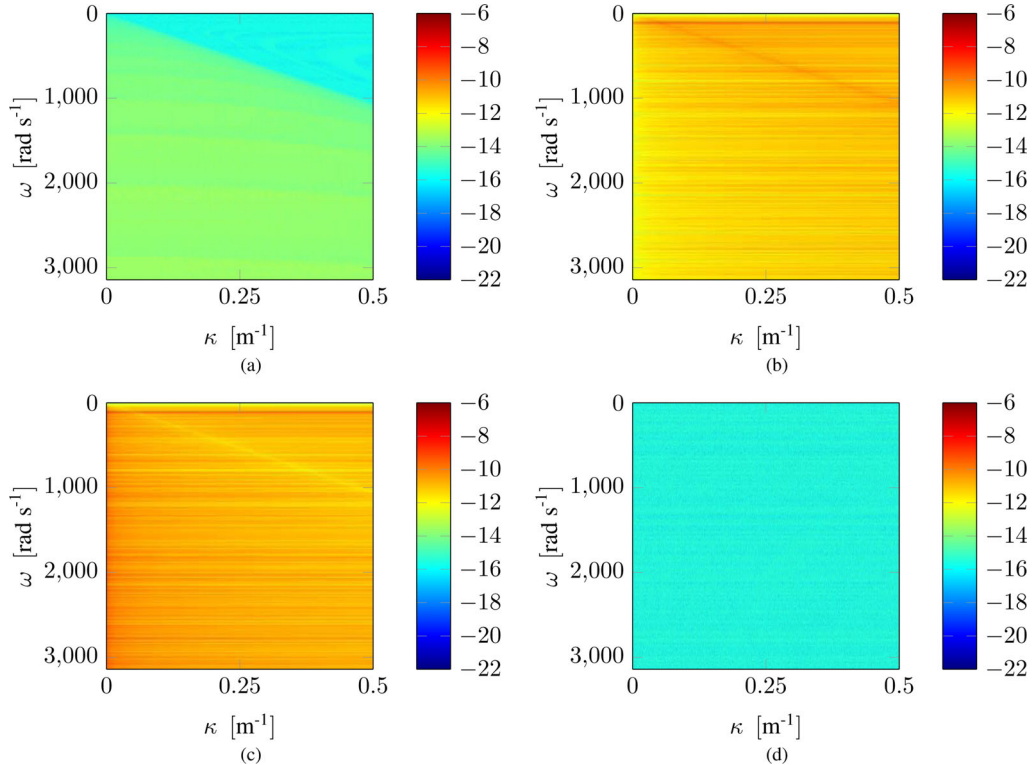
Figure D4. V2 identity check with the GST set for all radial wavenumber–angular frequency combinations. (a) Submatrix element (1,1); (b) submatrix element (1,2); (c) submatrix element (1,3); (d) submatrix element (1,4); (e) submatrix element (2,1); (f) submatrix element (2,2); (g) submatrix element (2,3); (h) submatrix element (2,4); (i) submatrix element (3,1); (j) submatrix element (3,2); (k) submatrix element (3,3); (l) submatrix element (3,4); (m) submatrix element (4,1); (n) submatrix element (4,2); (o) submatrix element (4,3); (p) submatrix element (4,4).

## APPENDIX E: FLUX-NORMALIZATION IDENTITY TEST USING HPF EIGENVECTORS

This appendix shows the results of the flux-normalization identity tests according to eq. (111), for H1 and V1, and eq. (112), for H2 and V2, respectively. These tests were carried out using the HPF eigenvector sets.
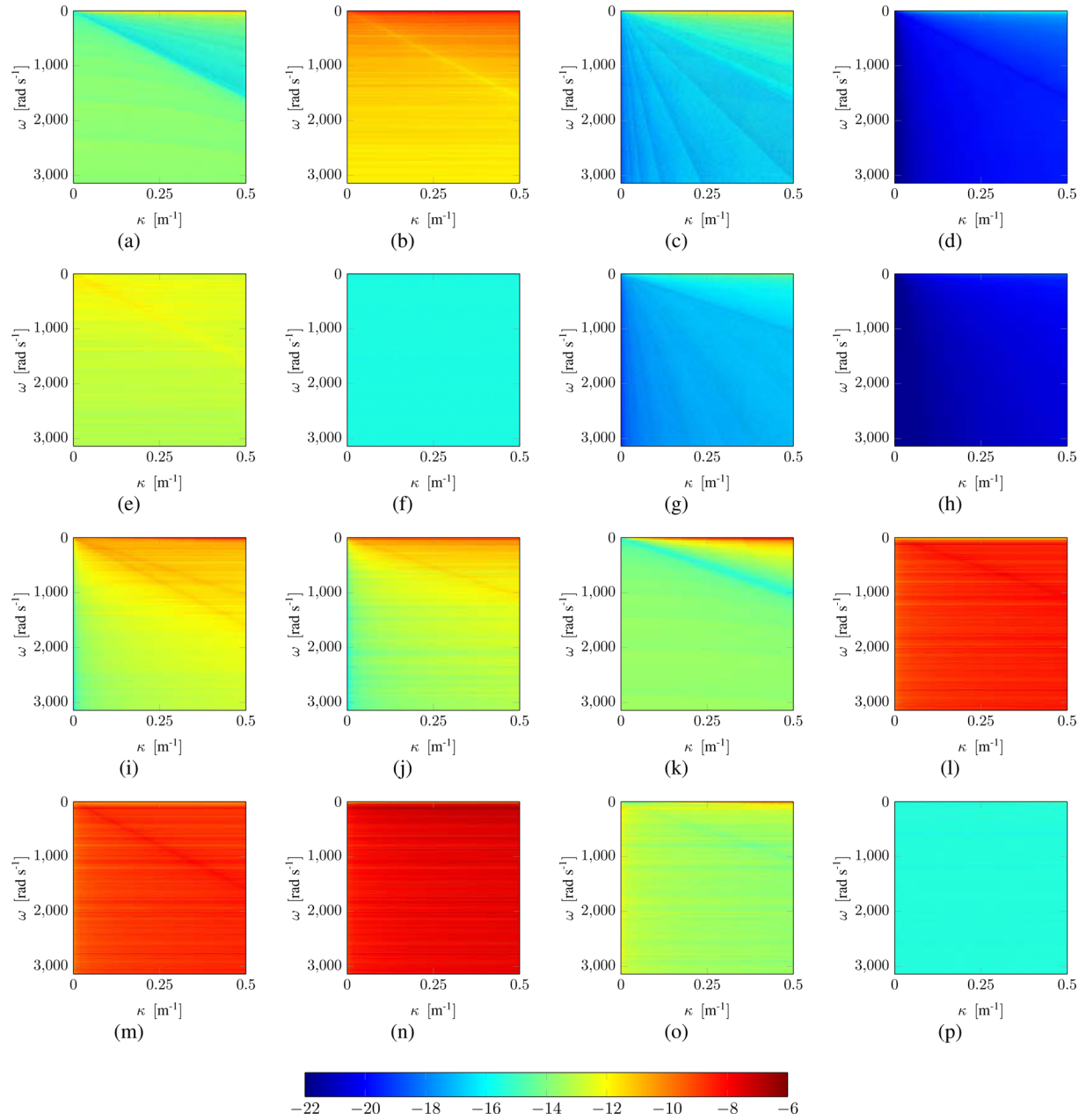

Figure E1. H1 identity check with the HPF set for all radial wavenumber–angular frequency combinations. (a) Submatrix element (1,1); (b) submatrix element (1,2); (c) submatrix element (2,1); (d) submatrix element (2,2).

Figure E2. H2 identity check with the HPF set for all radial wavenumber–angular frequency combinations. (a) Submatrix element (1,1); (b) submatrix element (1,2); (c) submatrix element (2,1); (d) submatrix element (2,2).
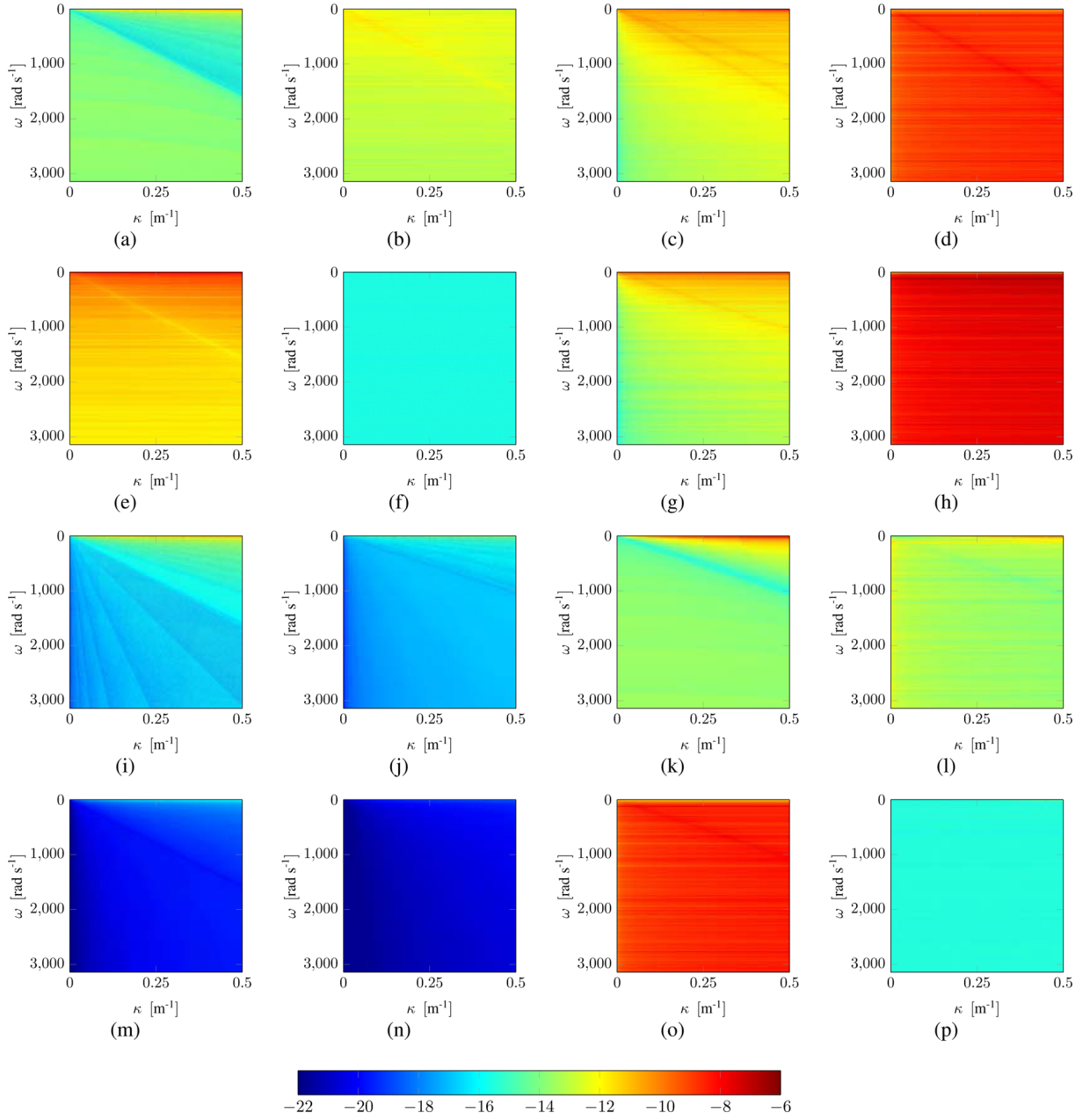
Figure E3. V1 identity check with the HPF set for all radial wavenumber–angular frequency combinations. (a) Submatrix element (1,1); (b) submatrix element (1,2); (c) submatrix element (1,3); (d) submatrix element (1,4); (e) submatrix element (2,1); (f) submatrix element (2,2); (g) submatrix element (2,3); (h) submatrix element (2,4); (i) submatrix element (3,1); (j) submatrix element (3,2); (k) submatrix element (3,3); (l) submatrix element (3,4); (m) submatrix element (4,1); (n) submatrix element (4,2); (o) submatrix element (4,3); (p) submatrix element (4,4).

Figure E4. V2 identity check with the HPF set for all radial wavenumber–angular frequency combinations. (a) Submatrix element (1,1); (b) submatrix element (1,2); (c) submatrix element (1,3); (d) submatrix element (1,4); (e) submatrix element (2,1); (f) submatrix element (2,2); (g) submatrix element (2,3); (h) submatrix element (2,4); (i) submatrix element (3,1); (j) submatrix element (3,2); (k) submatrix element (3,3); (l) submatrix element (3,4); (m) submatrix element (4,1); (n) submatrix element (4,2); (o) submatrix element (4,3); (p) submatrix element (4,4).